RAPID RECONNAISSANCE METHODS OF INVESTIGATION FOR TRACE COMPONENTS IN DEEP-SEA SEDIMENTS

by

Christopher David Bradbury

A thesis submitted to the faculty of
The University of Utah
in partial fulfillment of the requirements for the degree of

Master of Science

in

Geology

Department of Geology and Geophysics

The University of Utah

December 2012

The University of Utah Graduate School

STATEMENT OF THESIS APPROVAL

The thesis of **Christopher David Bradbury**

has been approved by the following supervisory committee members:

Richard D. Jarrard	, Chair	**8/13/2012** Date Approved
Erich U. Petersen	, Member	**8/16/2012** Date Approved
Peter H. Roth	, Member	**8/16/2012** Date Approved

and by **D. Kip Solomon** , Chair of

the Department of **Geology and Geophysics**

and by Charles A. Wight, Dean of The Graduate School.

ABSTRACT

Rapid reconnaissance methodologies are useful in investigations of deep-sea sediments, as they require little time for analysis and small amounts of sample material. This is especially useful for new studies of old cores drilled decades ago, which have become quite depleted. Both **Q**uantitative **E**valuation of **M**inerals by **SCAN**ning electron microscopy (QEMSCAN®) and handheld X-ray Fluorescence (XRF) instruments are ideally suited for such studies, as samples can be as small as 1 cc, and both are capable of rapidly detecting trace components within these small samples. Such speed allows multiple core horizons of interest to be analyzed for studies in paleoclimatology, extraterrestrial fluxes, and sediment velocity.

Grain-size and mineralogy of Ocean Drilling Program (ODP) Hole 722B are investigated using QEMSCAN® and compared to standard methodologies. QEMSCAN®-based grain-size, which indicates changes in paleowind strength due to the Indian Ocean summer monsoon for the last 200 ka, correlates well with previous data. Mineralogy is found to not correlate as well, however: dolomite has a good correlation, clays and feldspars a medium correlation, and quartz a poor correlation.

Handheld XRF is used for rapid reconnaissance of LL44-GPC3 and Canterbury Basin sediments from IODP Leg 317. Nickel-rich sediments are found in LL44-GPC3 at ~11.1 mbsf and ~12.4 mbsf, corresponding to layers known to have extraterrestrial nickel-rich spinel and known impact events at Chesapeake Bay and Popigai. Canterbury Basin sediment elemental peak counts are compared to velocity measurements of the same sediment, to establish the first conclusive

demonstration of carbonate cementation increasing velocities in siliciclastic sediments. For each sample, the handheld XRF measurement establishes its position on the sand-shale continuum, as well as the relative amount of calcite cementation. Determination of cementation occurring in porous sands with high velocities is shown, and linked to fluid flow in the region. Both studies illustrate the usefulness of handheld XRF as a reconnaissance methodology for detecting extremely subtle mineralogical signals within deep-sea sediments.

TABLE OF CONTENTS

LIST OF FIGURES

LIST OF TABLES

ACKNOWLEDGMENTS

First and foremost, special thanks go to my wife, who has helped me in numerous ways on this thesis, be it with her time or the temporary loss of her husband. A very special thanks to my mom and dad, without whose support I would not have pursued a career in academia.

I would especially like to acknowledge the assistance of Dr. Richard Jarrard, of the University of Utah, for both financial support and research assistance throughout the entirety of this thesis. Without Dr. Jarrard's support, this research would not have happened, and I would not be a graduate student. Rich has been like a father for me throughout this entire project, and has been very supportive of my goals in academia, and for this I am eternally grateful.

I also would like to thank the Energy and Geoscience Institute at the University of Utah for the use of their facilities and QEMSCAN® machine. Special appreciation also goes to Dr. Nick Dahdah of the Energy and Geoscience Institute, and his assistance and insight into QEMSCAN® sample preparation and analysis.

I would like to share my appreciation for my other committee members, Dr. Erich Petersen and Dr. Peter Roth, who both provided research assistance and support for this research. Special thanks as well to Drs. Y. Arakawa and Shigako Nigi, as well as other curators of the IODP Kochi Core Center for ODP Site 722 samples and assistance. Finally, special thanks to my fellow students and professors not named, who have helped me with numerous tiny details – you know who you are – thank you.

CHAPTER 1

INTRODUCTION

Nearly three-fourths of the Earth's surface lies beneath the oceans. Recent research in microbiology even suggests that life itself may have originated from the oceans (Martin et al., 2008). It is no surprise, then, that marine geology has been an important aspect of the geosciences, with some researchers going so far as stating that there is no geology without it (Kuenen, 1958). Of particular interest, in recent years, is the study of deep-sea sediments (Rea, 1994) and the glimpses they offer of Earth's recent geological past, and even far future. Using cutting edge techniques, researchers are able to tease out proxy data, such as grain-size for paleoclimate studies, find evidence of bolide impacts using extraterrestrial debris, and even determine cementation effects on sediment velocity. The first part of this study is focused on using **Q**uantitative **E**valuation of **M**inerals by **SCAN**ning electron microscopy (QEMSCAN®) to determine the median grain-size of dolomite and quartz from Ocean Drilling Program (ODP) Site 722B, Owen's Ridge, in the NE Indian Ocean. Earlier studies found nearly all terrigenous grains from the site to be eolian in origin (Clemens and Prell, 1991; Krissek and Clemens, 1991; Rea, 1994), making the site ideal for the investigation of QEMSCAN® as a useful methodology for grain-size analysis. The goal is to show that grain-sizes of eolian components from the site can be determined, and that data collected are comparable to previous research. Mineralogy is

also touched on briefly to see if similar signals to the work of Krissek and Clemens (1991) can perhaps be teased out using QEMSCAN®.

The second portion of this study investigates the possibility of using the Bruker handheld X-ray fluorescence instrument (handheld XRF) to locate core horizons with extraterrestrially sourced Ni-rich spinel, via measurement of nickel counts in the LL44-GPC3 Central North Pacific core. Nickel is common in meteorites but rare in the Earth's crust, and it is indicative of a bolide impact event sending debris into the Earth's upper atmosphere. Previous work (Pierrard et al., 1999) found high concentrations of Ni-rich spinel crystals at 11.1 m (2600 per mg) and 12.4 m (140 per mg) within this piston core. As the spinels are Ni-rich, the number of nickel counts on the handheld XRF data should be higher when compared to other portions of the same core. These locations in the core have been dated using ichthyoliths using the stratigraphy proposed by Doyle and Riedel (1979), and found to correlate to the Oligocene and late Eocene/early Oligocene, respectively, by Pierrard et al. (1999). The latter is coeval with the finding of Ni-rich spinel crystals at Massignano, Italy (Pierrard et al., 1998), as well as high concentrations of Ni-rich spinel crystals from ODP Hole 689B, Deep Sea Drilling Project (DSDP) Site 94, and DSDP Site 612, indicating widespread debris from possibly multiple bolide impacts.

The third and final part of this study delves into using handheld XRF data to investigate cementation effects on velocity from the Integrated Ocean Drilling Program (IODP) Leg 317 Canterbury Basin sites, offshore New Zealand. Lithologic and diagenetic parameters are determined from the elemental data provided by the handheld XRF, and their effects on velocity analyzed.

This thesis is organized as follows. Chapter 1 provides a brief introduction to the theory behind using eolian dust for paleoclimatic studies, with special emphasis on using grain-size to

determine paleowind intensity. Examples are drawn from multiple studies to provide a clear understanding of the subject. The chapter also introduces the study of bolide impacts and Ni-rich spinel crystals in deep-sea sediments as indicators of said impacts. Finally, the chapter concludes with a section on cementation, and its effects on the velocities of siliciclastic sediments. Chapter 2 describes the methods used for the investigation of the various sites in this thesis, with descriptions and theory to explain the use of QEMSCAN® and handheld XRF technology. Chapter 3 provides the analysis and evaluation of data from ODP Hole 722B, and the results of using QEMSCAN® to determine the grain-size and mineralogy of terrigenous particles. Chapter 4 reviews the validity of using handheld XRF as a tool for detecting evidence of bolide impacts using nickel counts as indicators of Ni-rich spinel within the sediments. Chapter 5 covers handheld XRF use as a rapid reconnaissance technique for investigating cementation effects on velocity in Canterbury Basin, offshore New Zealand.

1.1 Eolian Dust

The study of eolian dust is not new. In the mid-nineteenth century, Charles Darwin published a short paper on dust in the Atlantic Ocean (Darwin, 1846), and Maury devoted an entire chapter to the subject in his book, The Physical Geography of the Sea (Maury, 1855). The realization that these windblown sediments are found in deep-sea sediments did not come to the attention of the scientific community until the Challenger Expedition of 1872-76. Nearly a hundred years later, the importance of eolian dust as a component of Tertiary pelagic sediments was recognized (Heath, 1969). In this seminal work, Heath investigated the mineralogy of eolian grains from the northern equatorial Pacific, and found them to be dominated by minerals of continental origin. Further research into the field led to the development of paleoclimatic records

and models of past atmospheric circulation patterns (Lisitzen, 1972; Leinen and Heath, 1981; Sarnthein et al., 1982; Rea et al., 1985; Clemens and Prell, 1990; Rea, 1994; Kohfeld and Harrison, 2001). More recent research has even delved into dust's effects on climate change, biogeochemistry, and insolation receipt (Arimoto, 2001; Maher et al., 2010).

1.1.1 Dust Potential

It is now accepted that eolian dust grains are the best proxy for past atmospheric circulation, as they reflect both wind strength and provenance (Rea, 1994). The fine mineral grains that make up eolian dust are sourced from chemical and mechanical weathering, as well as volcanism. A geochemical equation of the breakdown of orthoclase to kaolinite and quartz is given as a simple example of chemical weathering below.

$$2KAlSi_3O_8 + 2H^+ + H_2O \xrightarrow{yields} 2K^+ + Al_2Si_2O_5(OH)_4 + 4SiO_2 \qquad (1.1)$$

A simple illustration (Figure 1.1) shows that the amount of dust created is dependent upon climate and the amount of water available (Pye, 1989; Rea, 1994). The more wet the source climate, the less dust produced. The more arid the climate, the more dust produced, except in hyperarid regions (Goudie, 1983; Prospero et al., 1989). This has been confirmed via modern observation of the African Sahel and Sahara Desert, where eolian dust production is found to be inversely correlated to the amount of rainfall the regions receive and to even increase in times of drought (Middleton, 1985; Nicholson, 1985).

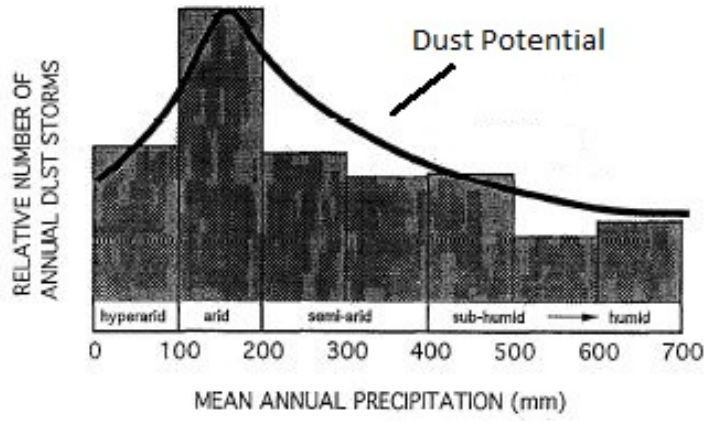

Figure 1.1. Illustration of dust potential. Note how dust potential increases with less precipitation and vice versa. Modified from Pye (1989).

1.1.2 Grain-Size

The size of eolian grains is reliant upon wind strength (Janecek and Rea, 1985; Rea, 1994; Arimoto, 2001). Traditionally, studies portray this concept using Stoke's Law of settling to determine the settling velocity of a spherical particle:

$$V_S = \frac{2(\rho_s - \rho_f)}{9*\eta} * g * r^2 \tag{1.2}$$

where V_S is the settling velocity, ρ_s is the density of the particle, ρ_f the density of a fluid, η the viscosity of the fluid, g the gravitational acceleration due to gravity, and r the radius of the particle. Using this information, the length of time a grain will remain in the atmosphere or ocean can be determined. It should be noted, however, that Stoke's Law models are developed for nonequilibrium transport, whereas grain-sizes are in equilibrium with their transporting winds (Rea, 1994). With equilibrium transport in mind, Janecek and Rea (1985) developed a

semiquantitative method of relating grain-size to wind intensity based on research by Gillete et al. (1974). This one-dimensional model has diffusion and sedimentation in equilibrium, and the diffusion coefficient as a linear function of height. This leads to the concentration with height being described using the following equation

$$\frac{\partial}{\partial z}\left(kU_* \frac{\partial c}{\partial z}\right) + V_s \frac{\partial c}{\partial z} = 0 \tag{1.3}$$

where k is von Karmann's constant (~0.4), U_* the friction velocity, z the height from ground, V_s the Stokes sedimentation velocity, and c the concentration of dust. For boundary conditions $c = c_0$ for $z = z_0$ and $c = 0$ as z goes to infinity

$$c = c_0 (\frac{z}{z_0})^{V_s/kU_*} \tag{1.4}$$

where c_0 is the initial concentration of dust and z_0 the reference elevation. This implies that when wind strength is greater than the settling velocity of a particle, the particle stays in the air for a longer time. Within a sediment core, this is observable as an increase or decrease in terrigenous grain-size through time, and is indicative of an increase or decrease in wind strength, respectively.

These implied changes in wind strength provide a proxy for ancient wind intensity. The size of the grains, as discussed earlier, provides this proxy, and grains are measured in Φ units, and are reported as the median grain-size (Φ_{50}) (Rea, 1994). The conversion from Φ to median grain-size (Φ_{50}) utilizes the negative logarithm to base 2 in the following equation:

$$-log_2 D_{mm} \quad (1.5)$$

where D is the diameter of the grain in millimeters; this leads to larger grains having a smaller Φ size. As such, 10Φ = 1 μm, 9Φ = 2 μm, 8Φ = 4 μm, 7Φ = 8 μm, 6Φ = 16 μm, and so forth (Rea, 1994). Once the eolian grain-size has been determined, wind intensity for various climatic events can be calculated (Gillete et al., 1974; Janecek and Rea, 1985). This has been demonstrated in the Pacific, where terrigenous grain sizes decrease in core LL44-GPC3 at a depth equivalent to the early Eocene, suggesting a decrease in overall intensity of atmospheric circulation, coinciding with more humid climates worldwide (Janecek and Rea, 1983; Rea et al., 1985). Studies linking grain-size to stronger monsoons in the Arabian Sea have also been conducted (Clemens et al., 1991; Rea, 1994), and it is found that stronger monsoons bring larger grains to the Arabian Sea at ODP Site 722 on Owen Ridge. This has been used to show that the Arabian Monsoon's strength is not dependent solely upon glacial-interglacial variability (Clemens et al., 1991), but rather on the cross-equatorial transport and release of latent heat with monsoonal rains as happens currently (Li and Yanai, 1996).

1.1.3 Mineralogy of Eolian Dust

The mineralogy of eolian dust differs based on the source region (Johnson, 1979; Rea et al., 1985; Brust and Waniek, 2010). The mineralogy is often determined using x-ray diffraction techniques (Till and Spears, 1969) or other methods (Brust and Waniek, 2010), which are fairly accurate (Rea et al., 1985). The mineral assemblages of the eolian dust can then be compared to possible source regions, and the area whose paleoclimate is represented ascertained. The mineralogy of eolian dust is also an indicator of aridity and humidity for the source climate (Rea,

1994). An example of this was investigated at ODP Site 722 (Krissek and Clemens, 1991), where it was determined that there are four mineral assemblages. Three important minerals found in the assemblages, chlorite, illite, and palygorskite, form via chemical weathering in arid and hyperarid regions, but break down via the same processes if moisture increases (Dixon and Weed, 1977; Velde, 1985; Krissek and Clemens, 1991). Another mineral found dominating its own assemblage, smectite, indicates humid conditions, as moderate chemical weathering is needed for its creation (Velde, 1985). This example illustrates clearly how mineralogical associations reveal information about the paleoclimate, which in turn can be tied to dust potential, and further to grain-size of terrigenous particulates and paleowind intensity.

1.1.4 Study Site Selection

As hemipelagic and biogenous sediments may obscure the desired eolian signals, locations to avoid them are the best places for study. Hemipelagic sediments may be deposited hundreds of kilometers offshore, well beyond any source river's deltaic fan and away from the continental shelf. This happens because the sediments may travel through the water column as a plume in the open ocean (Rea, 1994). These hemipelagic sediments are easily mistaken for eolian lithogenic components, as their composition and grain size may be similar if from the same source region. To avoid these pitfalls, eolian study areas need to be where hemipelagic shelf sediments cannot reach. Ideal locations are the centers of large oceanic gyres or regions of high altitude on the sea floor, such as volcanic ridges, which can rise thousands of meters above any reworked shelf and/or any hemipelagic sediments. It also helps if the uplifted areas are aligned parallel to any source regions, and perpendicular to the prevailing winds (Clemens and Prell, 1991; Stuut et al., 2002). The opaline silica and calcium carbonate shells of planktonic

organisms must be necessarily removed or avoided (Rea, 1994), as they also can be mistaken for terrigenous particles in some analytical methods.

1.2 Bolide Impacts

When an extraterrestrial body, such as an asteroid or comet, impacts the Earth, catastrophe ensues. These events, termed bolide impacts by the geologic community, cause local destruction at the impact site, and may have further reaching effects upon the atmosphere and/or biosphere. Atmospheric effects include dust clouds (Farley et al., 1998) and significant climatological changes (Pope et al., 1994). Effects upon the biosphere are often linked to climatological change and may lead to biotic extinctions (Glass and Zwart, 1977; Glass et al., 1985), the most famous of which is the extinction of the dinosaurs (Alvarez et al., 1980). The recent impact of comet Shoemaker-Levy 9 into Jupiter illustrates just how destructive such impacts can be to a planetary system (Weaver et al., 1995). Understanding past effects of such impacts on Earth has thus taken on new importance, with the realization that many near-Earth objects have the potential to crash into Earth.

Evidence for such events, however, can be difficult to locate, due to the Earth's ever changing surface. Erosion buries or destroys impact craters, and debris becomes mixed with terrestrial sediments. Some comets and meteorites even explode in the atmosphere, as seen in the 1908 Tunguska event (Chyba et al., 1993), leaving little evidence in the geologic record. As such, recent research of bolide impacts has focused on the strewn fields of impacts, consisting of the glassy ejecta known as tektites. Tektites are unique geologic tracers that are key indicators of bolide impacts.

1.2.1 Tektite Description and Formation

Tektites are generally spheroidal in shape and have a glassy appearance, with some even appearing droplet-like in shape (Vonhof and Smit, 1999). Once thought to have been from lunar volcanism (O'Keefe, 1970), research from the Apollo lunar missions refuted this, showing that tektite chemistry is distinct from that of lunar maria basalts (Taylor, 1973). Of particular interest to marine geologists are microtektites (tektites < 1 mm in diameter), which are found in deep-sea sediments. Of these, microkrystites (clinopyroxene bearing microtektites) are of particular interest as they contain nickel-rich spinel (Pierrard et al., 1999; Vonhof and Smit, 1999). As nickel is rare in Earth's crust and abundant in meteorites, it is believed that nickel-rich spinel forms via fusion and oxidation in Earth's atmosphere from molten droplets ablated from meteoritic material (Robin et al., 1992; Gayraud et al., 1996; Pierrard et al., 1999; Vonhof and Smit, 1999).

1.2.2 Tektite Chemistry and Implications

The chemistry of tektites reflects the chemistry of the source material, with losses during fusion restricted to elements more volatile than cesium (Taylor, 1973), with elemental abundances and interelement variations similar to terrestrial sandstones. The aforementioned meteoritic components of tektites, as well as high-pressure phase coesite, a mineral found at impact sites (Chao et al., 1960), provide evidence that tektites' origin is impact related. Four geochemically distinct tektite-strewn fields have been found and dated: Bediasites (North America/Pacific, 34 ma), moldavites (Czech Republic, 14 ma), Ivory Coast (1.3 ma), and Southeast Asian and Australian fields (0.7 ma).

Taylor (1973) further describes how the moldavites are likely linked to the Ries Crater event, and the Ivory Coast tektites are linked to the Bosumtwi Crater, Ghana by chemistry, isotope, and age. The North American strewn field's tektites appear to be sourced from the Chesapeake Bay impact crater (Vonhof and Smit, 1999), and although chemically similar, the Pacific strewn field tektites appear to be linked to the Popigai, Siberia crater. Maud Rise, ODP Hole 689B, microtektites are chemically dissimilar from both impact sites, indicating a third possible impact event in the Late Eocene (Glass and Koeberl, 1999; Vonhof and Smit, 1999).

1.3 Cementation Effects on Siliciclastic Sediments

It is well known that porosity is the primary variable controlling velocity in siliciclastic (sand-shale) sediment (Wyllie et al., 1956). It is also well documented that compaction, both mechanical and chemical, increases velocity in sediments by reducing porosity and/or increasing framework stiffness via increasing intergrain contacts (Figure 1.2) (Stoll, 1989; Erickson and Jarrard, 1998).

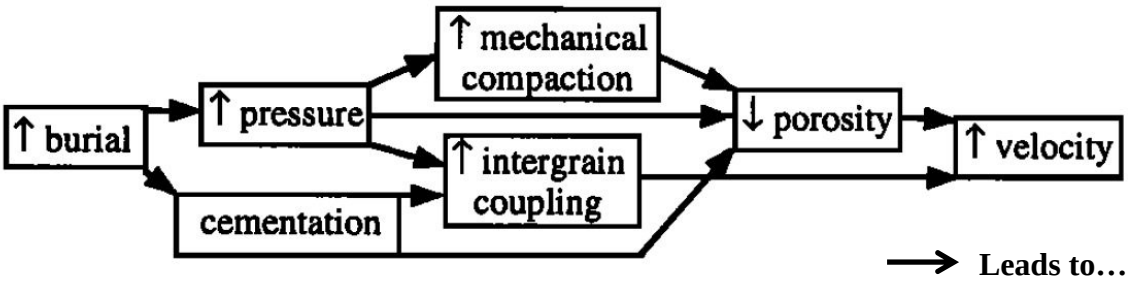

Figure 1.2. Effects on sediment velocities after burial. Note how increasing pressure and/or cementation leads to decreasing porosity and increasing velocity. Modified from Jarrard et al. (2000).

Mechanical compaction occurs due to effective stress on siliciclastic sediments leading to increasing overburden stress, and is controlled primarily by the mineralogy of the sediment. This is due to mineralogy controlling the geo-mechanical properties of sediments, including compressibility and stability. For example, quartz-rich sands show less compaction than lithic (rock fragment) sands (Chuhan et al., 2002), as the coarse, angular, and poorly-sorted lithic sands are more compressible (Friedman and Sanders, 1978). Regardless, mechanical compaction leads to the mechanical reorientation of grains, via breakage, compression, and sliding. This increases effective stress, which despite being partially compensated for by hydrostatic pressure from pore fluids (Terzaghi's Law), reduces pore space, leading to an increase in sediment velocity.

Whereas mechanical compaction is largely controlled by mineralogy, chemical compaction is also controlled by temperature. This is due to usually slow diagenetic reactions occurring rapidly at high temperatures, leading to dehydration, dissolution, precipitation, or recrystallization. It should be noted, however, that carbonate precipitation is an exception to this rule, as it can occur at low temperatures. Such diagenetic reactions can change the velocity of siliciclastic sediments significantly, as demonstrated by the process of cementation.

1.3.1 Cementation

In general, sand and shale compaction mechanisms and trends are different, with sand porosity decreasing gradually with depth (Taylor, 1950), and shale porosity decreasing rapidly as their "cardhouse" fabric is pressed into a parallel arrangement (Magara, 1980) via mechanical compaction. However, at depths greater than 1-2 km, chemical compaction, or diagenesis, becomes the dominant form of porosity reduction in sediments (Hayes, 1979; Foscolos, 1990; Hutcheon, 1990), and processes such as cementation, dissolution, precipitation, and

recrystallization occur. The diagenetic process of interest, cementation, is concentrated in sands. This is due to the higher permeability and consequently higher fluid flow in sandy sediments, which more readily allows precipitation of carbonate to occur.

Such impacts of cementation on velocity, however, were not persuasively seen in a dataset, until the investigation of Hole CRP-2 at Cape Roberts, Antarctica by Jarrard et al. (2000). The CRP-2 core consists of interbedded sandstones, mudstones, and diamicts (glacially-derived sandstones), and is drilled to a depth of 625 mbsf (CRST, 1999; Jarrard et al., 2000). The core has high porosities ranging from 0.1-0.4 (Niessen et al., 2000), and is located in a structurally active region with extensive, deep-seated, fluid flow (Jarrard et al., 2000), making it ideal for studies of porosity/velocity relationships due to cementation.

At the CRP-2 core, it is found that velocity increases up to 4 km/s at depths of 440-480 meters below sea floor (mbsf) (Jarrard et al., 2000; Niessen et al., 2000); when compared to the average of 2-3 km/s for the core, this is a sharp increase in velocity. As the increase in velocity correlates with an increase in carbonate cementation (Jarrard et al., 2000; Niessen et al., 2000) and does not appear to be due to lithology (Jarrard et al., 2000), it can only be due to increased intergrain coupling enhanced by carbonate cementation (Jarrard et al., 2000; Niessen et al., 2000). Evidence supporting this claim is found in CRP-2 sediments lacking significant porosity and velocity rebound, suggesting that rebound is being suppressed by said carbonate cementation (Jarrard et al., 2000). Furthermore, such high velocities in such high porosity sediments are much larger than those observed in uncemented Amazon Fan sediments (Erickson and Jarrard, 1998), leaving a depth-dependent increase in cementation as the only reasonable explanation for the porosity/velocity trends observed at the CRP-2 core (Jarrard et al., 2000). However, neither this

study nor others were able to demonstrate a direct linkage and correlation between amount of cementation and velocity increase within a single siliciclastic sequence.

CHAPTER 2

INSTRUMENTS AND METHODS

In this study, multiple instruments and methodologies are used. Energy-dispersive X-ray spectroscopy (EDX) is the analytical technique employed by both QEMSCAN® (Gottlieb et al., 2000) and the Bruker AXS Tracer III-V+ and III-SD handheld X-ray fluorescence (XRF) devices (Nazaroff et al., 2010). Due to the oversampling of many deep-sea cores, the small amount of material necessary for these analyses makes these instruments ideal for this study. A custom velocimeter measures acoustic wave velocity of Canterbury Basin cores, which is then compared to elemental data gathered using the Bruker AXS Tracer III-SD XRF, to determine mineralogical trends of interest.

2.1 QEMSCAN®

Quantitative **E**valuation of **M**inerals by **SCAN**ning electron microscopy, colloquially known as QEMSCAN®, is FEI Company's descendant of the QEM*SEM developed by CSIRO. The QEMSCAN® Automated Mineralogy system uses a scanning electron microscope (SEM), with up to four EDX spectrometers. EDX spectra and backscattered-electron image (BEI) are obtained from each x-y point in a raster scan pattern, to identify the chemical composition of a sample's surface. These data are then compared with a hierarchical mineral database, known as a

Species Identification Protocol (SIP), within the iDiscover® software suite. Elements that must be present, elements that may be present, and the BEI are all used to select the mineral that best fits the spectra (Gottlieb et al., 2000; Haberlah et al., 2010).

Despite the effort that has been put into achieving system ergodicity for automated mineralogy solutions (Jenkins et al., 1995), limitations for electron microbeam technology still exist. According to Gottlieb et al. (2000), X-ray generation volume is only 1 to 2 microns across, with sample penetration depth approximately the same at 25 keV operation voltage. This implies that X-rays for mineral phases beneath the phase of interest can be generated and skew results. The analysis time is 1-2 milliseconds per spot, meaning that the speed versus detection limit tradeoff is such that elements present in amount of ~ < 5 weight percent are not detected. The size of particles is also of concern. Particles of diameter 5 microns or less have insufficient points for accurate representation (Gottlieb et al., 2000), although modern technology with resolution of 1 micron has reduced this error significantly. Stereological bias is also possible, and is dependent upon texture. Significance of this error can be determined and dealt with using careful mathematical analysis if needed (King and Schneider, 1998).

2.1.1 Sample Selection and Preparation

Grain-size analysis of eolian sourced deep-sea sediments requires a location with specific parameters. Any site for investigation must be free of fluvial sourced hemipelagic sediments, which is difficult, as they can travel hundreds of kilometers offshore as a plume in the water column (Rea, 1994). This means areas uplifted above reworked shelf sediments, such as volcanic ridges which may rise thousands of meters above such sediments, are ideal for study. The ridge being parallel to any source region and perpendicular to the prevailing winds is also important

(Clemens and Prell, 1991; Stuut et al., 2002). ODP Site 722 in the Arabian Sea is located on Owen Ridge, and meets the aforementioned requirements (Clemens and Prell, 1991). The site is also ideal because of the effects of the Arabian Sea summer monsoon. Strong winds and the nearby Arabian Desert produce a large flux of eolian dust to the northwest Arabian Sea, Owen Ridge, during the summer monsoon season (McDonald, 1938; Prospero, 1981). This makes it relatively simple to examine lithogenic dolomite and quartz grain-size at the ODP site.

Sample horizons for investigation in the core are selected from throughout Hole 722B to sample multiple points in the past. However, as the core was depleted from previous research, the core repository sent material available for one-cc sample size. This limited core samples to 26 samples, with most being from the middle to bottom portion of the core. One-cc samples were chosen, due to the ease of using such small volume for QEMSCAN® study, and the aforementioned depletion of the core being investigated.

Samples are prepared by crushing core plugs using mortar and pestle into a fairly homogenized powder of small particles. This ensures that grains of interest are distributed randomly throughout any sample scanned by the instrument. The mortar and pestle are cleaned using highly filtered ionized water after each use, and the lab workstation kept clean to avoid contamination. After storage and cataloging, samples are then mounted using a carbon tape methodology. Crushed sample is placed on carbon tape mounted on a 30 mm diameter acrylic pellet. Excess sample is removed via compressed air, and samples labeled appropriately.

2.1.2 Sample Mounting Techniques

QEMSCAN® data are collected under vacuum, and samples need to be stable under such conditions. Unstable samples may break apart, damaging fine instrumentation and destroying

experiment integrity. For the fine-grained deep-sea sediments of the Hole 722B core, multiple sampling techniques were investigated.

Sample stages for the instrument can hold 30 mm sample plugs, with smaller plugs being fit using custom machined steel adapters, if necessary. Carbon-coated epoxy plugs with impregnated samples are the primary means of investigation for QEMSCAN®, and these were the initial method of choice for this investigation. However, after several samples were made, it was discovered that sediment would settle as the epoxy hardened. Pressed pellets made of boric acid were then created with a thin film of mixed sample powder and boric acid on the surface. It was found that if pure sample powder were pressed to the boric acid pellet surface, it often would later spall off. In contrast, a mix of ~50:50 sample:boric acid maintained pellet rigidity. However, the sample press led to pellets having 31 mm diameter, requiring sanding of samples down to the 30 mm diameter of the QEMSCAN® sample holder. This often caused destabilization of pellets, and some would shatter under stress. The surface of boric acid pellets also did not remain stable under vacuum at times, and particulates entered the vacuum chamber of the instrument. An acrylic rod was then cut into approximately 12.7 mm sections, and a few drops of epoxy with sample placed on the surface. To avoid the settling issue, sanding of the surface was attempted. However, this often led to unacceptably low concentration of sample at the surface.

Using double-sided carbon tape has the advantages that it prevents charging, requires no carbon-coating, and its bottom sticky surface readily attaches to the aforementioned acrylic rod segments. One-cm wide double-sided carbon tape is placed on the acrylic plug, from edge-to-edge to ensure that any charge returns to the sample stage. Powdered sediment is then sprinkled on the carbon tape, until an even coat is established on the surface. Excess sediment may be

removed via compressed air and/or by tapping it off. The samples remain stable under vacuum, and no particulate separation is observed. Using this method proved to be an efficient and viable means of sample preparation, and is ultimately the method chosen for this study.

2.1.3 Analysis Techniques

Analyses were done at the Energy and Geoscience Institute at the University of Utah Research Park using a QEMSCAN® 4300, with a Zeiss EVO 50 SEM platform. This instrument uses four Bruker X-Flash® energy dispersive X-ray detectors to collect elemental spectra. Prior to each analysis, the instrument calibration is performed, as outlined by Ayling et al. (2012). An accelerating voltage of 20 keV and specimen current of ~5 nA is used during instrument operation. Data are collected using iMeasure® v. 5.2 beta software, in field-scan mode, at one micron spacing, for a 400 x 400 micron field image at the center of each sample.

Data are processed using iDiscover® 5.2 beta software, using the Oil and Gas v. 3.3 SIP. The granulator and touching particles processors are used to extract dolomite and quartz grain data, and the area percent of each dolomite and quartz grain is then used to determine the diameter of each grain, and exported to Kaleidagraph® and Microsoft Excel® software, where median grain-size for each sample is determined and patterns investigated.

2.2 Bruker AXS Tracer III Series Handheld XRF Instruments

The Bruker AXS Tracer III-V+ and III-SD series of handheld XRF instruments provide analytical capabilities similar to a bench-top instrument (Nazaroff et al., 2010), using advanced X-ray detector technology, as well as proprietary S1PXRF software to control current and voltage for the instrument, and ARTAX software to process elemental data. This is accomplished

by bombardment of a sample with X-rays from an X-ray tube with an Rh target with emission up to 40 keV (Sendova et al., 2010). The bombardment excites electrons in atoms, and can lead to the ionization and ejection of an electron, releasing a photon with energy unique to the element from which it is radiated (Goldstein et al., 2002; Cesareo et al., 2009). The emitted spectra are then collected using Bruker's proprietary X-Flash® Silicon Drift Detector (SDD), and processed using proprietary software. Escape peaks due to elastic scattering and Compton scattering are both detected and compensated for within the software (Cesareo et al., 2009). The portability of these energy-dispersive X-ray spectroscopy systems has led to applications in multiple fields of the sciences, including archaeology (Nazaroff et al., 2010; Speakman et al., 2011), art (Marabelli et al., 2005; Cesereo et al., 2007), environmental sciences (Rhodes, 1971), mineralogy (Cesereo, 1997), and planetary geology (Economou et al., 1996).

2.2.1 Sample Selection and Preparation

Portability allows XRF samples to range from an outcrop or rock in the field, to powders and small rocks in the laboratory. As such, sample selection and preparation differs for each experiment. In this case, samples from the Equatorial Pacific LL44-GPC3 core are prepared and sampled quite differently than samples from the Canterbury Basin, offshore New Zealand.

2.2.1.1 LL44-GPC3

Samples for LL44-GPC3 are selected partly based on core horizons known to contain microtektites from previous research efforts (Pierrard et al., 1999). Samples from near those horizons and distant from them are also chosen to ensure that data gathered are representative of the piston core along its length.

The experiment endeavors to detect high nickel X-ray counts, indicative of microtektites. As such, each core plug is crushed into a homogenized powder to ensure even distribution of material, as any nickel spectra detected will be reflected back to the detector from the surface of powder scanned. Crushing is accomplished via mortar and pestle, which are cleaned using highly filtered ionized water in the laboratory.

2.2.1.2 Canterbury Basin, New Zealand

Sample selection for the Canterbury Basin samples is done using the same parameters as Brusova (2010). Samples scanned are the same samples for which velocimeter data are collected, making for consistent comparison of the two datasets. This also allows cementation effects to be established using both elemental and velocity data.

Core plugs are scanned without being crushed for this scan, and are the same samples used by Brusova (2010) for velocity measurements. As the samples are still wet with seawater, and have some honey, used as couplant in the velocity experiment, great care was taken to ensure no damage is done to the XRF instrument.

2.2.2 Analysis Techniques

Samples from LL44-GPC3 are analyzed using the Bruker AXS Tracer III-V+ instrument using thin-film analysis. First, the crushed powder was placed in Bruker sample cups, with 4 micron thick plastic barrier between the sample and handheld XRF. After each sample run, any residual sample in the sample cup was removed using compressed air, or by replacement of plastic.

Analysis for Canterbury Basin core plugs was carried out using the Bruker AXS Tracer III-SD instrument. As the core plugs are saturated with sea water from velocity measurements, each sample was placed on a piece of wax paper to protect the instrument. After each sample run, the wax paper was replaced to prevent sample contamination.

Data for each run are collected at a Baud rate value of 115200, using the pdz setting for obsidian. An operating voltage of 15 keV was used, as was an actual anode current of 28 μA. No filter was used in either study. Samples from LL44-GPC3 were scanned for 5 minutes to collect maximum X-ray counts for nickel, which is present in very low concentrations. For Canterbury Basin samples, where major elements are the objective, samples were scanned for 90 seconds.

Data were then processed using ARTAX software, where spectra are processed, and elemental data teased out. Each element detected by the XRF must be marked in the software, so that proper processing occurs. It should also be noted that multiple gathered sample spectra may be processed simultaneously, allowing processing to be complete in minutes. Processed data is then exported to Microsoft Excel® or Kaleidagraph® software for manipulation and/or creation of graphs. Further details can be found in the ARTAX software user manual available from Bruker.

2.3 Velocimeter

Acoustic wave velocities for Canterbury Basin core samples are measured using a custom made velocimeter, designed specifically for determination of P and S wave velocities versus pressure. The equipment consists of a hydraulic pump, oscilloscope, pressure vessel, transducer assembly, and a transducer controller. The velocimeter allows for the collection of in situ and atmospheric velocity measurements for each recovered core sample of interest.

2.3.1 Sample Measurements

Sampling interval is approximately 50 meters on recovered core. Selection is based on the multisensor track, the need for minimal disturbance of core, and being adjacent to index property measurements for calculation of all elastic moduli (Brusova, 2010). Samples are 1 inch diameter cylinders, kept saturated in seawater, and may be lithified or unlithified. For measurement of velocities as a function of pressure, a sample is placed between the two transducers of the velocimeter, and the entire transducer assembly is then enclosed in a pressure chamber. The hydraulic pump then pressurizes samples at half in situ pressure, in situ pressure, half in situ pressure, and then atmospheric pressure. This is done to ensure hydrostatic pressure is achieved for each measurement, and is dependent upon whether coupling is sufficient for adequate signal strength. Some samples were measured only at atmospheric pressure, outside the pressure vessel. The oscilloscope and its software are then used to capture P and S wave velocities for each sample.

2.3.2 Analysis Techniques

The P and S wave velocity arrival times are picked by the operator using the oscilloscope captured waveforms. The P-wave velocity of the sample (V_p) is calculated from the first arrival for the P-wave traveltimes (TT_{total}) by

$$V_p(meters/sec) = L(meters)/(TT_{total} - TT_{transducers})(sec) \quad (2.1)$$

where L is the length of the core sample, and $TT_{transducers}$ = 12.410 μsec the P-wave travel time correction for a P-wave travelling between two transducers without any sample inserted. Brusova

(2010) analyzed V_p at in situ pressures, and compared V_p at in situ pressures to V_p at atmospheric pressures. In this study, the focus is on V_p at atmospheric pressure, which is compared to elemental data gathered using the handheld XRF.

CHAPTER 3

QEMSCAN® ANALYSIS OF LATE NEOGENE SEDIMENTS, ODP SITE 722, NORTH-WEST INDIAN OCEAN

Grain-size and mineralogy are well established proxies for paleoclimate studies involving deep-sea sediments (Rea, 1994). These proxies reveal the general climatic conditions of the past, with grain-size being useful for paleowind strength, and mineralogy for paleoenvironment and source region. However, finding areas where such proxies provide reliable data can be difficult, as eolian signals may be easily obscured by fluvial sediment and/or organic processes. Owen Ridge is one such location, where grain-size and mineralogic proxies are able to illuminate past conditions, due to the ridge's location under Indian Ocean summer monsoon winds, and its unique depositional setting.

3.1 Indian Ocean Summer Monsoon

Indian Ocean summer monsoon winds are driven by the differential heating between the cold Indian Ocean and the warm India-Asia subcontinent. This leads to the development of high surface pressure (low pressure aloft) over the Indian Ocean and low surface pressure (high

pressure aloft) over the India-Asia subcontinent. This creates a northeast-southwest pressure gradient (Figure 3.1), which is strengthened by the "moist process," the release of latent heat over the continents by monsoon storms (Webster, 1987). From these processes, strong upper level winds of up to ~30 knots develop over the Arabian Sea, which when coupled with the nearby arid Arabian Peninsula provide a large flux of eolian dust up to 18.5 microns in diameter to the Arabian Sea (McDonald, 1938; Prospero, 1981; Ackerman and Cox, 1982; Prodi et al., 1983; Tsoar and Pye, 1987; Clemens and Prell, 1990, 1991). In fact, nearly 80 % of the terrigenous flux to the region occurs at this time and is eolian in origin (Nair et al., 1989). This is easily observed via haze at sea, which demonstrates that June, July, and August, the strongest

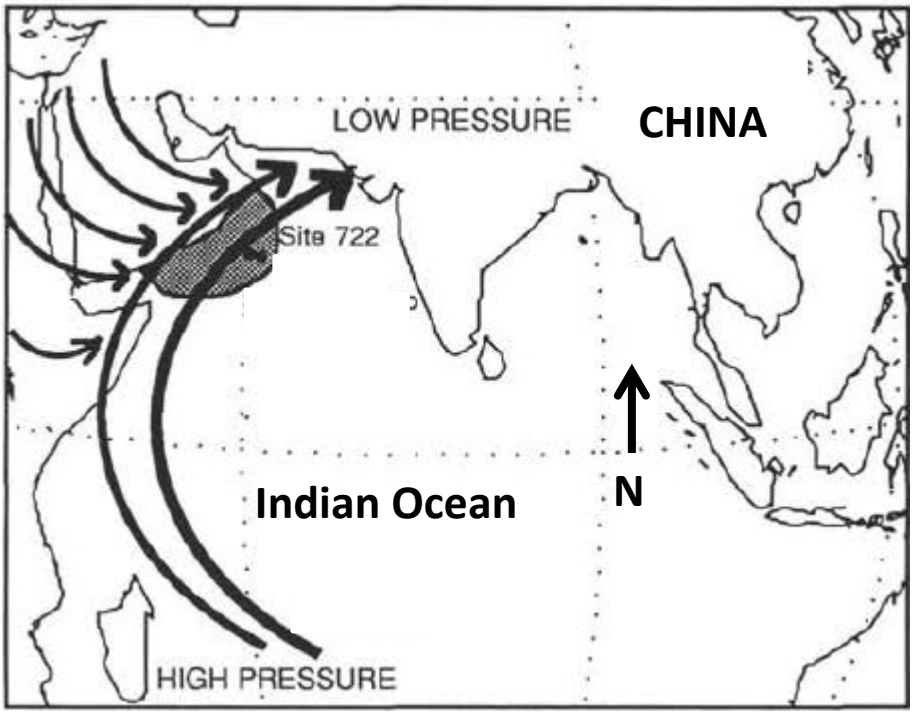

Figure 3.1. Location of ODP Site 722. The northeast-southwest pressure gradient created during the Indian Ocean summer monsoon. Modified from Clemens and Prell (1991).

summer monsoon months, are the primary months of aerosol transport from the southeast coast of Arabia to the Arabian Sea (McDonald, 1938; Prospero, 1981; Clemens and Prell, 1991). In the winter, the continents cool, reducing upper level winds to ~10 knots, and reversing their direction landward, rather than seaward (Hastenrath and Lamb, 1979).

In Earth's past, monsoon processes differed from the current climatic regime for the region. For example, glacial periods are exemplified by increasing aridity (Street and Grove, 1979; van Campo et al., 1982; Prell and van Campo, 1986; van Campo, 1986), decreased precipitation, and expansion of unvegetated terrain (Mahowald et al., 1999). In the Northwest Indian Ocean/Arabian Sea region, these conditions created stronger winter northeast trade winds and weaker summer monsoons, possibly with different trajectories than at present (Krissek and Clemens, 1991). These stronger winter winds led to an increase in grain-size (Rea, 1994), and 2-20 times greater sediment flux to the Arabian Sea (Mahowald et al., 1999).

Interglacials, on the other hand, show increased humidity and precipitation (Street and Grove, 1979; van Campo et al., 1982; Prell and van Campo, 1986; van Campo, 1986). These conditions led to reduced wind strength and smaller grain-size for dust aerosols (Rea, 1994). For the region around the Arabian Peninsula, the interglacial climate is dominated by strong summer southwest monsoon winds and increasing precipitation (Prell and van Campo, 1986).

3.2 Depositional Setting

Owen Ridge provides a unique opportunity to investigate the paleoclimate of the Arabian Peninsula and East Africa using eolian proxies, because of its geographical location and geomorphology. Owen Ridge is located 350 km off the coast of the Arabian Peninsula, running nearly parallel to the country Oman, placing the ridge directly beneath the axis of strong Indian

Ocean summer monsoon winds, and beneath any eolian aerosols that may settle out from these winds. The geomorphology of the ridge plays an important role in eolian signal preservation, despite complex depositional processes interacting in the region. This is due to the ridge rising 1500 meters above the Oman Basin to the northwest, and 2000 meters above the Indus Fan to the Southwest. Owen Ridge's uplift began in the Middle Miocene as shown by the in-core lithologic transition from turbidite deposits to pelagic carbonates, showing that the ridge was uplifted above the zone of turbidite and overbank deposition (Weser, 1974; Mountain and Prell, 1989; Shipboard Scientific Party, 1989; Clemens and Prell, 1991; Debrabant et al., 1991). These conditions make the ridge ideal for detection of eolian signals, as it rises above fluvial hemipelagic sediment entering the Northwestern Indian Ocean/Arabian Sea basin via the Indus River, which would obscure eolian signals in ridge sediments. The eolian sediments would be obscured, because Indus Fan sediments are rich in chlorite and illite due to derivation from the Himalayan Complex (Krissek and Clemens, 1991), are indistinguishable from eolian sediment transported from the Thar Desert of India (Kolla et al., 1981), and similar to Arabian Peninsula eolian sediments (Krissek and Clemens, 1991). This illustrates how, despite the Arabian Sea possibly having the highest recorded flux of eolian material in the global marine environment (Prodi et al., 1983; Chester et al., 1985; Savoie et al., 1987), analyzing the material is difficult unless the seafloor meets the aforementioned criteria.

3.3 Regional Paleoclimate

The relationship of Owen Ridge sediments to regional paleoclimate is in part determined by sediment's original source region. Terrigenous material's source region is determined using the unique mineralogic characteristics of the material, and then comparing that information to

known ancient and modern soils. This reveals not only ancient and modern wind patterns, but also the paleoclimatic and paleoenvironmental conditions of the region. Grain-size provides information on wind circulation and strength. Variations in grain-size occur as climate shifts, meaning that it reveals changes in monsoonal strength through time. Together, grain-size and mineralogy change through time from core horizon to core horizon, revealing the paleoclimatic conditions of a given geographical region.

Global Climate Model (GCM) studies (Kutzbach and Guetter, 1986) have linked increasing insolation to increased differential heating between the southern Indian Ocean and southern Asian continent. This differential heating creates stronger monsoon circulation (Kutzbach, 1981; Kutzbach and Otto-Bliesner, 1982; Kutzbach and Guetter, 1986; COHMAP Members, 1988) and therefore stronger winds capable of carrying larger grains of eolian dust. This can be enhanced by global ice volume increases during glacial periods, leading to decreased vegetative cover and increased deflation of lithogenic material via wind (Kukla *et al*., 1988). The uplift of the Himalayan complex also allows for latent heat to be released over the Asian continent, increasing the aforementioned pressure gradient of the monsoon. Other variations in the amount of global insolation, global ice volume, Indian Ocean sea surface temperature, and the albedo and elevation of the Asian continent also change the strength of monsoon circulation through time (Kutzbach, 1981; Kutzbach and Otto-Bliesner, 1982; Prell, 1984a, b), and provide climatic controls on grain-size.

Currently, the Arabian Sea is provided a significant amount of sediment from the deposition of eolian dust (Goldberg and Griffin, 1970; Kolla and Biscaye, 1977; Kolla *et al*., 1981). Study of the mineralogical distribution of eolian dust reveals that dust's ultimate origin from the surrounding geographical region. For example, sediment rich in chlorite and illite,

whose composition is similar to soils found in the Iran-Makran region, is found throughout the Arabian Sea (Kolla et al., 1976, 1981). Aerosols collected over the Arabian Sea during the northeast monsoon are transported by northerly and/or northwesterly winds (Krissek and Clemens, 1991) from the Iran-Makran region (Chester et al., 1985). Some chlorite and illite rich material may also be delivered to the Arabian Sea by northeast trade winds from the Thar Desert of India, but this component is too compositionally similar to Indus Fan sediments to be distinguished as its own signal (Kolla et al., 1981). The clay palygorskite has also been found in Arabian Sea sediments, derived from the palygorskite-rich soils of the Arabian Peninsula and Somalia via westerly and southwesterly winds (Clemens and Prell, 1991; Krissek and Clemens, 1991). Major sources of chlorite, dolomite, detrital carbonate, palygorskite, and smectite are also transported to the Arabian Sea by the summer northwesterly winds from Oman and Central Arabia (Sirocko and Sarnthein, 1989). Other mineralogic components of the Arabian basin include fluvially derived smectite from the Deccan Traps of India, and minor input of kaolinite from the tropical soils of Africa, Madagascar, and southern India (Krissek and Clemens, 1991).

Any climatic fluctuations in these source regions over geologic time scales affected the mineralogy of sediments derived from them (Krissek and Clemens, 1991). This occurs due to changes in precipitation, vegetation, and other environmental factors. During Pleistocene glacial periods, increased aridity of the source region led to the expansion of saline littoral, arid desert, and steppe inland environments. These environments are ideal for the creation of eolian dust and associated minerals that form under arid conditions such as chlorite, dolomite, illite, and palygorskite (Dixon and Weed, 1977; Velde, 1985; Krissek and Clemens, 1991). Interglacial periods, on the other hand, have increased humidity and precipitation (Prell and van Campo, 1986), in turn expanding environments covered by savanna-type vegetation (van Campo et al.,

1982). Such precipitation promotes chemical weathering, and minerals such as smectite are favored over arid mineralogic assemblages (Velde, 1985).

3.4 Previous Work

Extensive work has been done on ODP Site 722 (Clemens and Prell, 1991; Krissek and Clemens, 1991; Rea, 1994) and provides a wealth of information for comparative studies. Research of particular interest is that which focuses on grain-size and mineralogic relationships to the Indian Ocean summer monsoon. Comparison of this research to similar studies, such as this thesis, should yield similar results, and provide insights into the viability of new technologies for grain-size and mineralogy paleoclimate research efforts.

3.4.1 Grain-Size Analysis

Clemens and Prell (1991) investigated grain-size from Hole 722B using the University of Rhode Island Elzone Particle Analyzer (E.P.A.), measuring the volume of particles based on electrolyte displacement as lithogenic grains pass through an orifice (Clemens and Prell, 1990), without identifying individual mineral grains. This methodology reveals the grain-size record of ODP Hole 722B to be a high frequency record indicative of monsoon wind strength having a more complex response to climatic forcing mechanisms than aridity, implying that source region aridity is not dependent upon monsoon strength (Clemens and Prell, 1991). These findings suggest the grain-size record is externally forced by precessional insolation, and internally forced by interactions that occur between global ice volume and availability of latent heat, which help determine summer monsoon wind strength (Clemens and Prell, 1990). These relationships do not appear to have changed for at least the last one million years or so, other than a decrease in grain-

size beginning at 500 ka. This abrupt decrease in grain-size continues until the present, and suggests an overall decrease in stronger monsoon wind strength over the last half million years. However, these findings do not correlate to the *Globigerina bulloides* upwelling record, which is an independent record of paleowind strength (Anderson and Prell, 1991). This indicates a decoupling of the grain-size and *Globigerina bulloides* records prior to 500 ka, and that the observed decrease in grain-size may not be due to changing monsoon wind strengths, but rather due to a possible change in lithogenic source region. The loss of such a region may account for changes in grain-size without there being a change in wind strength, and may occur via changes in lofting potential of lithogenic dust or shifting wind patterns (Clemens and Prell, 1991). Such changes occurred during the Pliocene-Pleistocene orogeny of the Zagros Mountains and the associated development of the modern Persian Gulf (Kassler, 1973). These tectonic events could have influenced source region lithology, distribution, and local wind patterns, such as the northwesterly Shamal winds over Arabia (Pye, 1987). This may be a possible explanation, as the grain-size decrease does not appear to be related to vegetative changes due to aridity (Clemens and Prell, 1991). The overall grain-size record also shows little coherency with regards to the interactions of grain-size variations and insolation forcing, global ice volume, and latent heat processes with glacial/interglacial cycles (Clemens and Prell, 1991). However, coherency between Hole 722B and RC11-210 grain-size records in the equatorial Pacific point to a strong relationship of Indian Ocean summer monsoon strength and the Pacific Ocean southeast trades, and in turn insolation forcing (Clemens and Prell, 1991). Ultimately, the cause of grain-size change is still uncertain, and a likely explanation takes into account both insolation variation through time, as well as regional tectonic changes that affected lithogenic material carried out to Owen Ridge.

3.4.2 Mineralogical Analysis

Krissek and Clemens (1991) analyzed mineralogy of Owen Ridge sediments using X-ray diffraction for the last 500 ka, using the same samples as Clemens and Prell (1991). Using R-mode factor analysis of the mineral/boehmite peak ratio data, Krissek and Clemens (1991) determined the loadings for each mineral in each sample. These data were to be converted to quantitative mineral percentages using calibration curves as outlined in earlier research (Gibbs, 1967; Krissek, 1982; Scheidegger and Krissek, 1982); however, this proved impossible due to nonuniform grain-sizes throughout ODP Hole 722B samples (Krissek and Clemens, 1991). Due to this, only downcore variations in the peak ratio of each mineral could be presented, but comparison of two or more minerals was impossible (Krissek and Clemens, 1991).

Based on factor analysis, Krissek and Clemens (1991) successfully identified four unique mineral assemblages (Factors 1, 2, 3, and 4), with each factor consisting of a group of minerals, that provide information on the source region(s) as well as likely prevailing weathering conditions.

Factor 1 is defined by high loadings for chlorite, dolomite, and quartz. Chlorite is important to this assemblage, as it is formed in an arid region with minor chemical weathering (Dixon and Weed, 1977; Velde, 1985; Krissek and Clemens, 1991). Also pointing to an arid source climate is dolomite, which can be created via the desiccation of sabkhas (Dixon and Weed, 1977). Appropriate source lithologies for Factor 1 have been around for the last 500 ka and exist in Iran-Makran, Oman, the Arabian Peninsula, and East Africa. The mineral dolomite's presence in the assemblage points to its source being from the Arabian Peninsula and Oman, as dolomitic lithologies are exposed there (Sirocko and Sarnthein, 1989).

Factor 2 consists of illite, kaolinite, and plagioclase feldspar. Illite forms from the degradation of mica or via weathering of potassium feldspars under conditions of limited precipitation (Dixon and Weed, 1977; Blatt et al., 1980). These same conditions are also favorable for the preservation of plagioclase feldspar (Krissek and Clemens, 1991). In the last 500 ka, source lithologies in conditions of limited precipitation have existed for this assemblage in the Arabian Peninsula, Iran-Makran, and Somalia (Kolla et al., 1981; Sirocko and Sarnthein, 1989).

Factor 3 is dominated by smectite, a mineral that requires a climate of moderate chemical weathering (Velde, 1985). Under such climatic conditions, minerals such as plagioclase feldspar are unstable and are not preserved. Major sources of smectite to the modern Arabian Sea are the Deccan Trap basalts of India (Krissek and Clemens, 1991). However, suitable source rocks for the last 500 ka have been exposed in the Arabian Peninsula and East Africa (Kolla et al., 1981; Krissek and Clemens, 1991). These data point to Factor 3 smectite being blown over Owen Ridge from one of these locations over the time period of 500 ka to present.

Factor 4 minerals include dolomite and palygorskite (Krissek and Clemens, 1991). Palygorskite forms in marine environments, such as alkaline lakes, carbonate deposits, and evaporite deposits (Velde, 1985; Krissek and Clemens, 1991). Palygorskite degrades under even very minor chemical weathering, so it can only exist in regions of aridity. Source regions for palygorskite include the arid Arabian Peninsula and East Africa (Kolla et al., 1981; Sirocko and Sarnthein, 1989). The presence of dolomite, however, points to the source region being the Arabian Peninsula, where carbonate lithologies from which it can form are plentiful (Sirocko and Sarnthein, 1989).

In summary then, Factors 1 and 4 show sustained production of eolian dust to the Arabian Sea from the Arabian Peninsula and Oman, with Factors 2 and 3 being less well-defined regionally (Krissek and Clemens, 1991). Krissek and Clemens (1991) also found their interpretations of source climates complicated by the short-term variability of the mineralogical record. Their spectral analysis showed that Factors 1, 2, and 4 appeared to increase during the more arid glacial intervals (Krissek and Clemens, 1991), indicating that regional climatic shifts were an integral part of the reason for variations in mineralogy found in the core samples at Hole 722B, Owen Ridge.

3.5 QEMSCAN® Analysis Results

Data collected for this study provided a fairly robust sample suite for both grain-size and mineralogy: 25 of the 26 samples from ODP Hole 722B provide excellent data, with the exception being the sample from 0.84 meters depth, which has too few dolomite and quartz grains for analysis. All other samples have several hundred data points.

3.5.1 Grain-Size

Grain sizes for both dolomite and quartz are determined, as both minerals are known to be eolian in origin if found in Owen Ridge sediments (Clemens and Prell, 1991). Minus the core horizon 0.84 meters in depth, the samples each have several hundred grains available for analysis, allowing the median grain-size for dolomite, quartz, and the average of both to be calculated for 25 core horizons from ODP Hole 722B for comparison to the work of Clemens and Prell (1991) (Table 3.1).

Table 3.1

QEMSCAN® Grain-Size Diameter

Depth (m)	[a]Age (ka)	Dolomite (µm)	Quartz (µm)	[b]Average (µm)
0.44	11	3.9	3.9	3.9
1.44	27	4.2	4.2	4.2
2.04	39	4.2	3.9	4.0
2.44	47	4.2	3.9	4.0
2.64	51	4.2	4.2	4.2
2.84	55	3.9	3.9	3.9
3.24	65	3.9	3.9	3.9
3.44	69	4.8	4.8	4.8
3.64	75	3.9	3.9	3.9
3.84	81	4.2	4.8	4.5
4.04	91	4.2	4.8	4.5
4.24	100	4.8	4.2	4.5
4.44	110	4.2	3.9	4.0
5.24	130	4.8	3.9	4.4
5.74	138	3.9	4.8	4.4
5.94	142	4.8	3.4	4.1
6.14	145	4.8	5.5	5.2
6.34	149	3.9	4.2	4.0
6.94	159	4.8	4.2	4.5
7.14	163	3.9	3.6	3.8
7.34	166	4.2	4.2	4.2
7.54	170	4.2	4.2	4.2
7.74	174	4.8	4.2	4.5
7.94	179	3.9	4.2	4.1
8.14	184	4.8	4.2	4.5

[a]Dates are based on those given by Clemens and Prell (1991) and Krissek and Clemens (1991). They are only approximate.

[b]The average is the combination of both dolomite and quartz median grain-sizes, providing the lithogenic average for these two important minerals. This also allows analysis to be performed more easily, whilst still providing pertinent data on the eolian component of ODP Hole 722B sediments.

Downcore variations in both dolomite and quartz grain-size are observable from approximately 11 ka to 184 ka. Data lay within a 95 % confidence interval (Nair, 1940) for both dolomite (Figure 3.2a) and quartz (Figure 3.2b). The 95 % confidence interval shows that QEMSCAN® grain-size diameters are reliable for comparison to Elzone Particle Analyzer data collected by Clemens and Prell (1991). High median grain-sizes on this plot correspond to stronger paleowind strength, and low median grain-sizes to low paleowind strength.

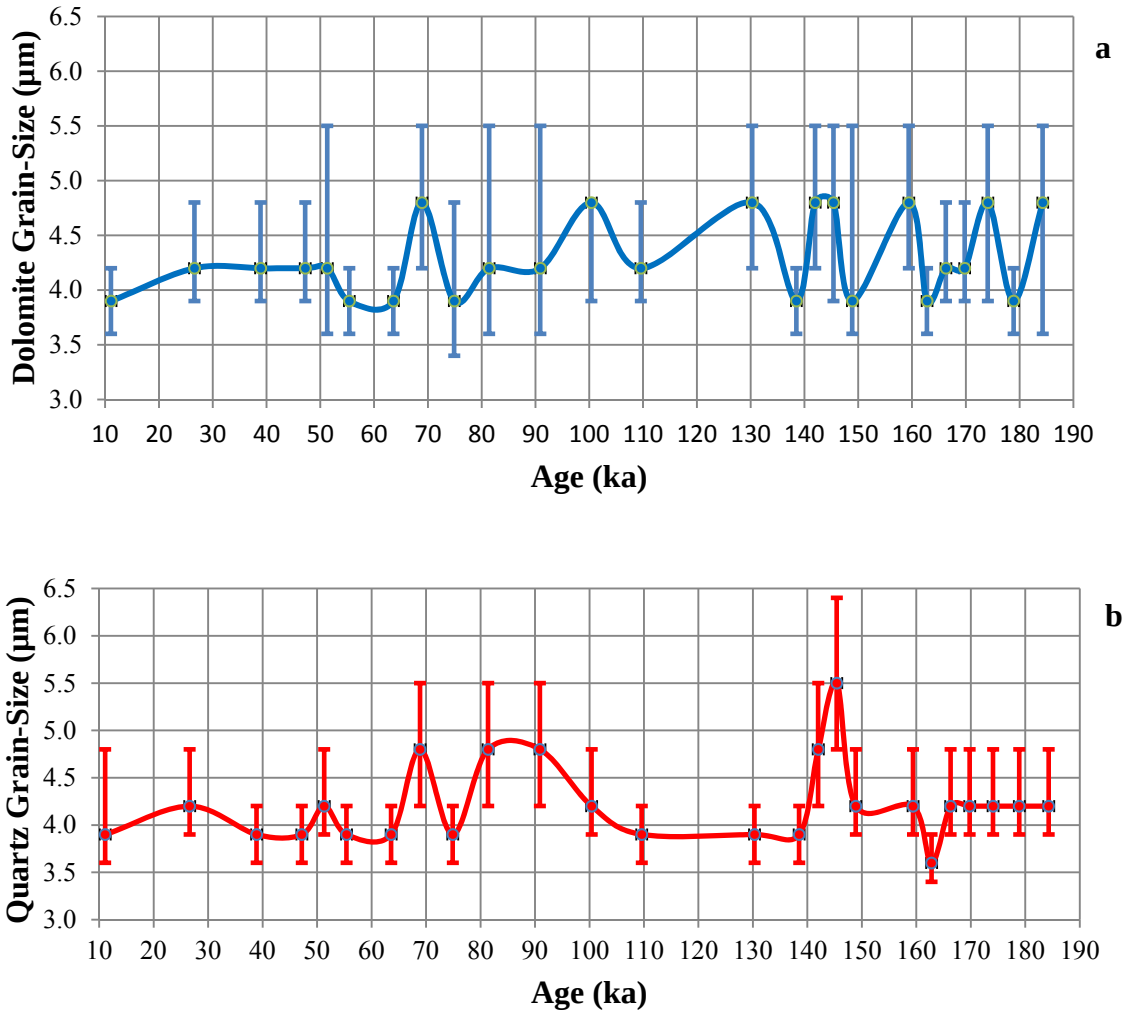

Figure 3.2. Dolomite and quartz median QEMSCAN® grain-sizes: **a** is dolomite grain-size diameter, and **b** is quartz grain-size diameter. Note the error bars illustrating the 95 % confidence interval for grain-size in the population.

The average of dolomite and quartz (Figure 3.3) median grain-sizes shows peaks at 27 ka, 51 ka, 69 ka, 81-100 ka, 130 ka, 145 ka, 160 ka, and 174 ka. Significant valleys, or decreases in grain-size, are observed at 55-64 ka, 75 ka, ~110 ka, 138 ka, 149 ka, 163 ka, and 179 ka. These data when compared to Clemens and Prell (1991) data show remarkable similarities, with the primary difference being solely median grain-size. This is surprising, especially as Clemens and Prell (1991) grain-size is greater than QEMSCAN®-observed grain-size by a factor of three. This is not likely due to an error in QEMSCAN® instrumentation, as a preliminary study found QEMSCAN® to accurately measure the size of Whitehouse Standard® silicon beads accurately. Various reasons for this discrepancy are possible, with differences in methodology being first and foremost. QEMSCAN® only extracted the data for individual dolomite and quartz grains, whereas the Elzone Particle Analyzer scanned all lithogenic material after calcite dissolution. Possibly, some clay flocculation biased the Elzone analyses. Regardless of the difference in size

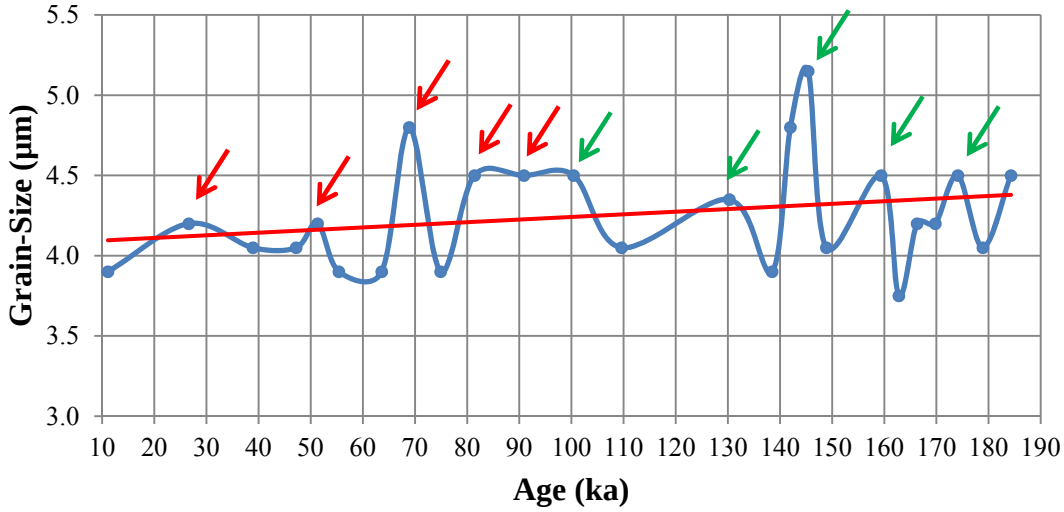

Figure 3.3. Average grain size for dolomite and quartz. Arrows show significant peaks, with red arrows showing correlation with glacial millennial climate events. Grain-size decreases toward modern times, as illustrated by the red trendline.

and instrument methodologies, the question still remains as to whether or not the paleoclimatological story being told is the same. To determine if this is indeed the case, two separate analyses are done.

QEMSCAN® data are scaled up by a factor of 3.6 to show any visual similarities between the two datasets (Figure 3.4). The two data sets appear to match each other well, with the exception of median grain-size from 145-130 ka, which seem to mirror one another. Despite how well the two data sets match, further analysis is performed in order to ensure that scotoma is not occurring. Derivative analysis shows if two datasets are similar, as locations in the data where the slope is zero will cross at the zero line. If the datasets are similar, these crossings should be equivalent or close when plotted. As shown (Figure 3.5), the datasets do indeed often meet at the zero line, or are only slightly offset from each other. In conjunction with the previous analysis, this suggests a similar paleoclimatological story is being told by both datasets.

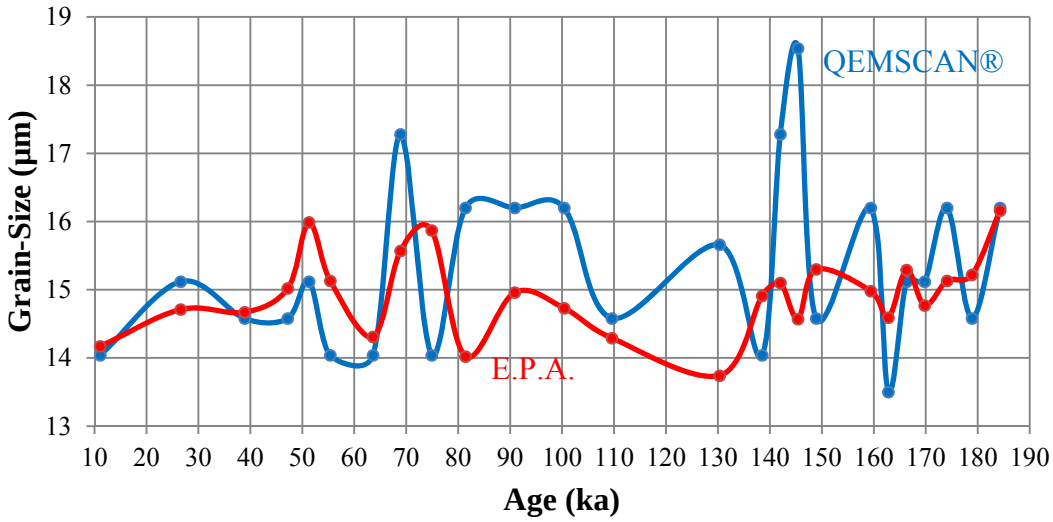

Figure 3.4. Comparison of normalized QEMSCAN® and E.P.A. grain-size results. The two datasets are visually similar.

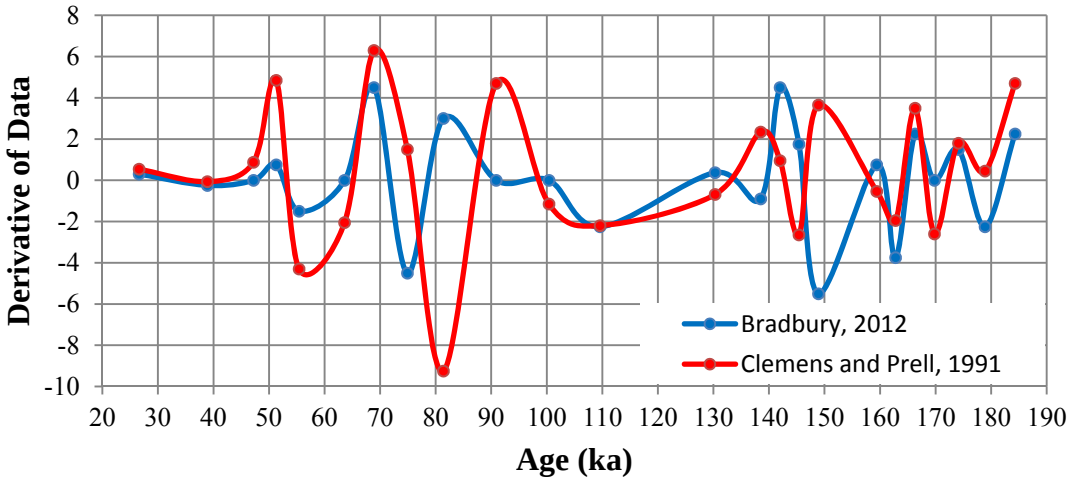

Figure 3.5. Derivative analysis of E.P.A. (Clemens and Prell, 1991) and QEMSCAN® (Bradbury, 2012) grain-size data. Note how often the two meet at zero, or are only slightly offset. This is indicative of a general correspondence of peaks and troughs in the two time series.

Clemens and Prell (1991) noted a long-term trend of decreasing grain-size toward the present time. As seen in Figure 3.3, that trend is also observed in the QEMSCAN® data, implying that a similar paleoclimatological story is being told by both datasets. The two techniques for determining grain-size yield generally similar results. QEMSCAN® may be preferable when available samples are very small or if a single mineral, rather than whole-rock analysis, is the focus of the analysis.

3.5.2 Mineralogy

Mineralogical analysis by the QEMSCAN® instrument shows each ODP Hole 722B sample to consist of ~80 % biogenic carbonate, consistent with previous work (Clemens and Prell, 1991), with much smaller percentages of clays, dolomite, feldspars, and quartz (Figure 3.6). As the species identification protocol (SIP) used by QEMSCAN® does direct mineralogical analysis of a sample's surface, area percent for each mineral can be calculated. Clays and

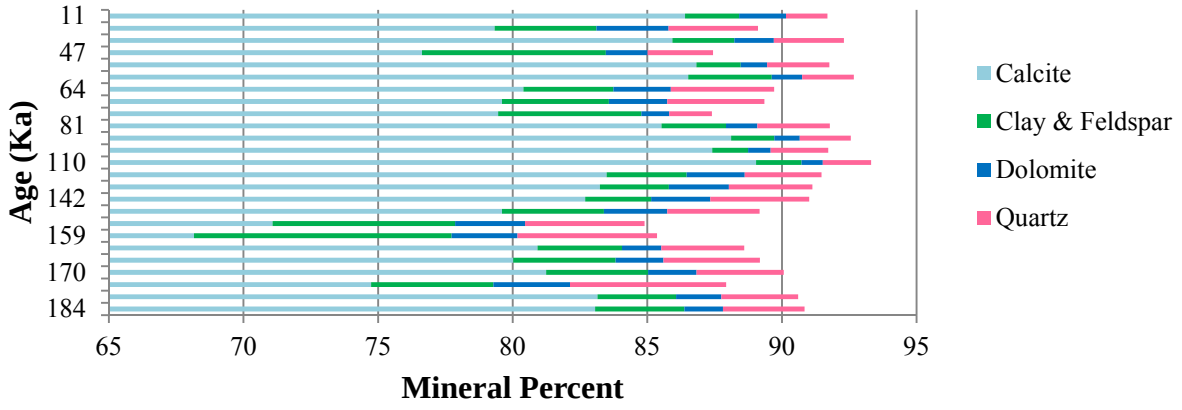

Figure 3.6. Mineral area percent for ODP Hole 722B. Graph begins at 65 %. Unreported data are background. Dates are approximate, and based on those given by Clemens and Prell (1991) and Krissek and Clemens (1991).

feldspars provide a limitation, however, as the SIP used cannot reliably distinguish between these two geochemically similar mineral groups. This is why, in this study, clays and feldspars are treated as one group. Dolomite and quartz, on the other hand, are each treated separately, as QEMSCAN® is able to distinguish between the two minerals accurately and consistently.

As QEMSCAN® area percent is a quantitative value and XRD data semiquantitative, similarities between the two datasets are determined using a somewhat qualitative analysis. QEMSCAN® mineral percentages, converted to a ratio of mineral percent/total noncalcite mineral percent and the X-ray diffraction (XRD) mineral/boehmite peak ratios, are semi-quantitatively compared using a double-Y plot. This analysis will allow for comparison of both old and new data, and in turn show whether downhole variations are similar or not as the XRD mineral/boehmite relative abundance should rise and fall with QEMSCAN® area percent.

This semiquantitative data analysis shows that clays and feldspars have some correlation, with the two methodologies having some similarities, but also substantial differences (Figure 3.7). Note how several of the peaks do align together, but from approximately 145 ka to 100 ka, the two datasets are nearly opposites of each other.

On the other hand, dolomite shows fairly good correlation, with data from the two methods matching or being very similar to each other at nearly every datapoint (Figure 3.8). Even most of the variation in abundance throughout the hole matches well, with rises and falls in dolomite concentration occurring simultaneously in both QEMSCAN® and XRD datasets. Even the significant increase in dolomite from 166 ka to 138 ka, and its subsequent decrease at 110 ka, is captured quite clearly by QEMSCAN® instrumentation.

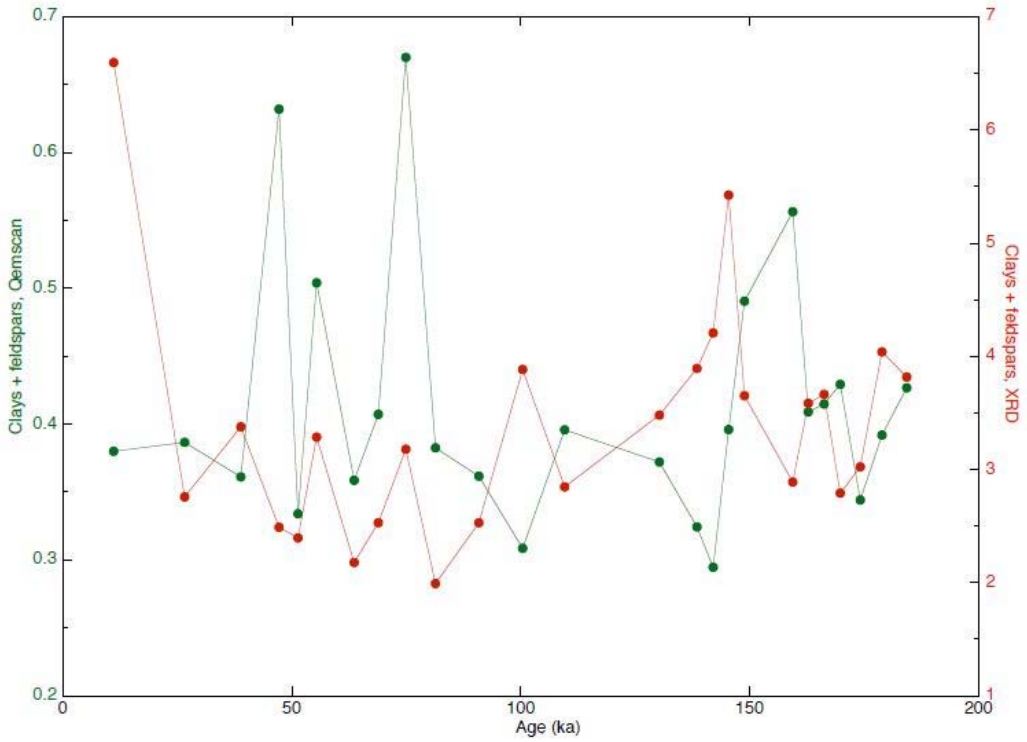

Figure 3.7. Comparison of QEMSCAN® area percent and XRD relative abundance for clays and feldspars by age.

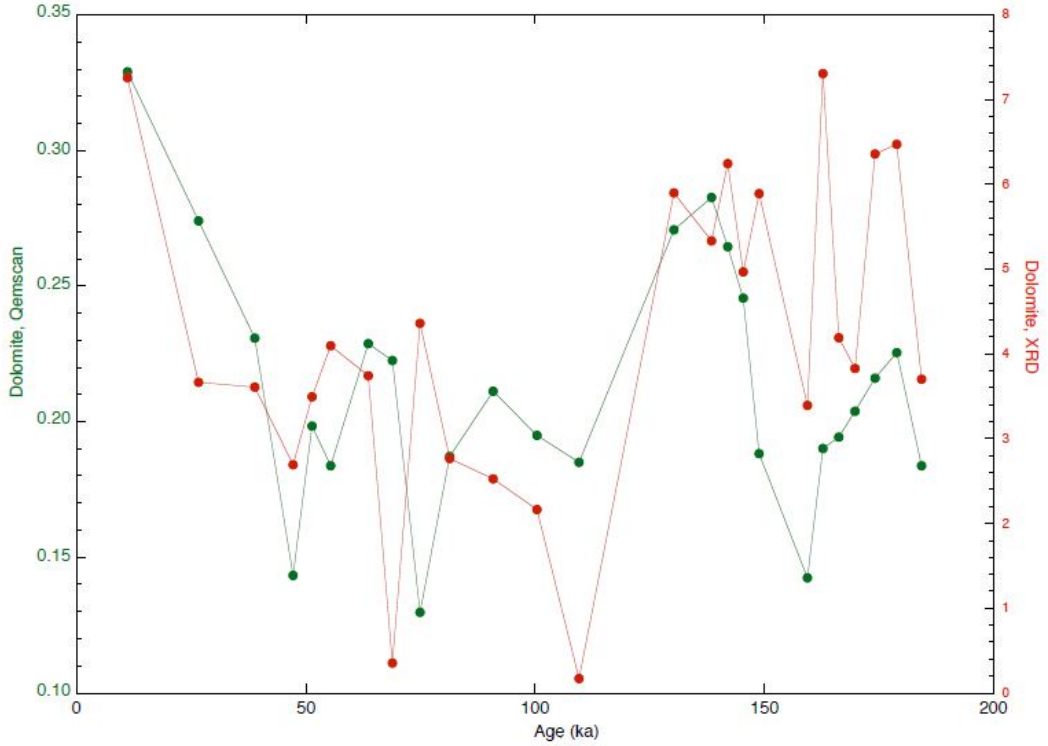

Figure
3.8. Comparison of QEMSCAN® area percent and XRD relative abundance for dolomite by age.

Quartz comparison is much like the clays and feldspars analysis. QEMSCAN® and XRD data do not correlate to each other, with the exception of some large increases or decreases in quartz content happening coeval to each other (Figure 3.9). With the exception of these apparent increases and decreases in abundance, QEMSCAN® data are characterized by much larger values than those observed via XRD. This leads to confusing results, as QEMSCAN® is reliable at detecting quartz. The cause of this is perhaps due to unremoved radiolarian material being detected by QEMSCAN®, which cannot distinguish mineralogically between quartz and hydrous opaline silica. Examination of the individual quartz grains shows that virtually all exhibit the rounded morphology expected of eolian sourced quartz; radiolarian and/or diatom morphologies were rarely observed.

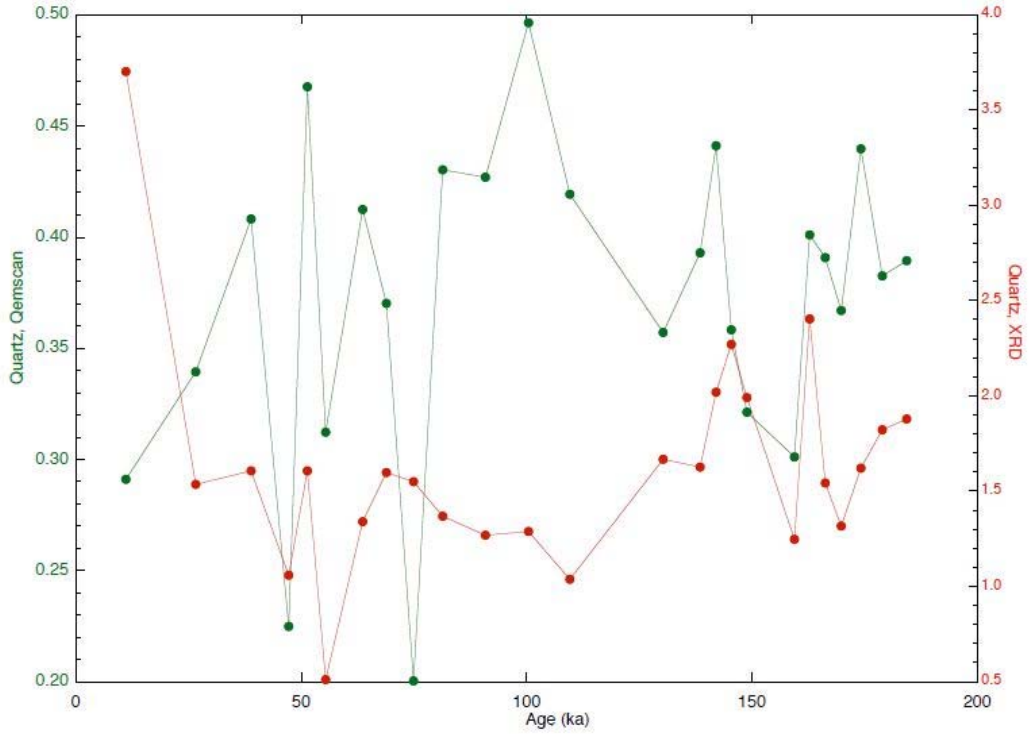

Figure 3.9. Comparison of QEMSCAN® area percent and XRD relative abundance for quartz by age.

Due to the semiquantitative analysis being inconclusive, crossplots for each dataset were created and linear regression fitted to each mineral assemblage to determine any significant correlation. The correlation coefficient (*R*) determines how well the variable datasets from QEMSCAN® and XRD match to each other. The crossplots and associated correlation coefficients show dolomite to lie within the 95 % confidence level (Fisher and Yates, 1948) for significant correlation, with an R value of 0.411 for 25 samples (Figure 3.10a). However, quartz (Figure 3.10b) and clays and feldspars (Figure 3.10c) show no statistically significant correlation, with R values of 0.168 and 0.066, respectively. These data show that either QEMSCAN® is detecting mineralogical changes not previously observed, or that dissolution of

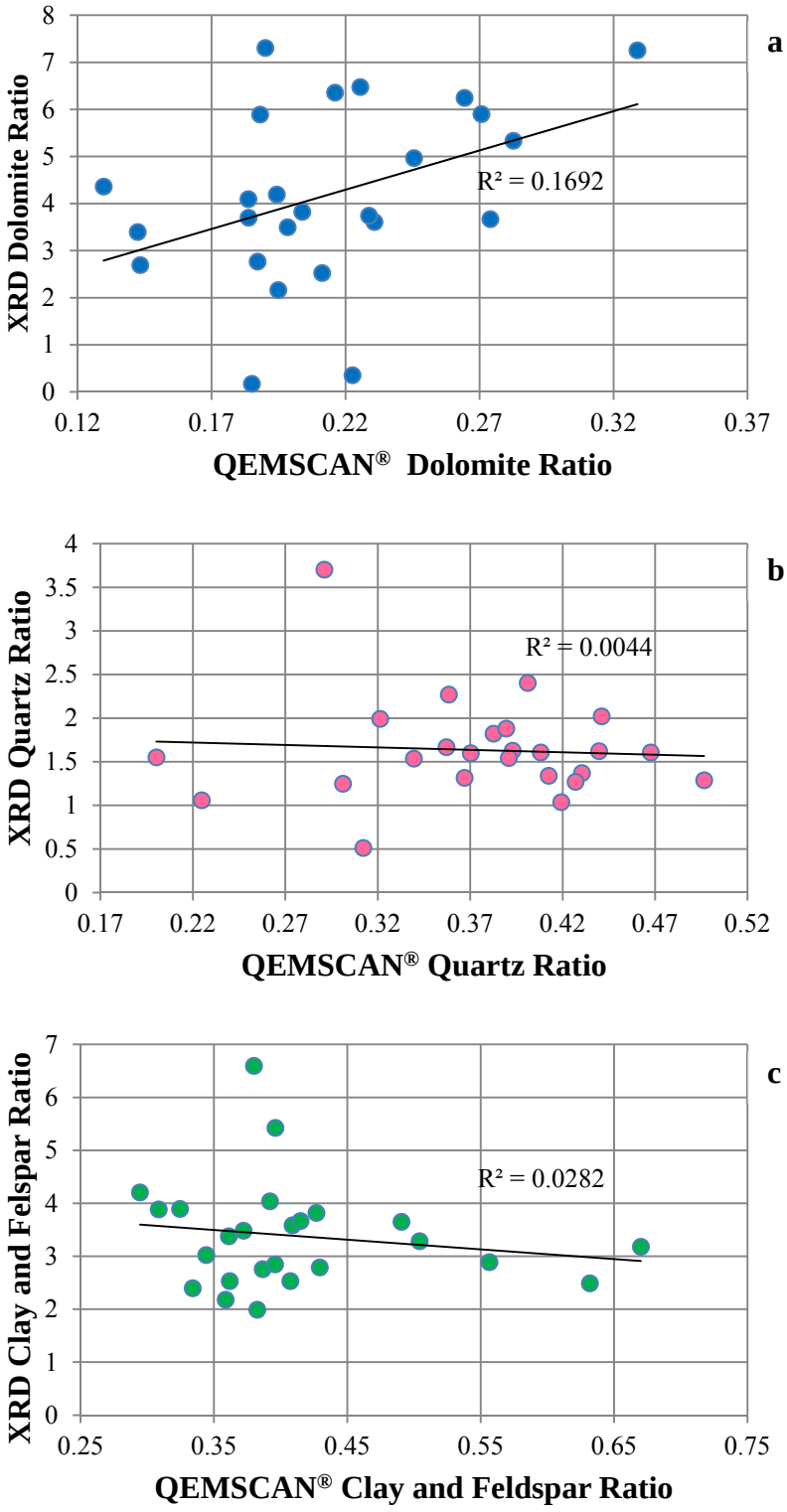

Figure 3.10. Crossplots of XRD and QEMSCAN® mineral ratios: **a** is dolomite, **b** is quartz, and **c** is clays and feldspars. The two dolomite datasets are significantly correlated at the 95 % confidence level, but quartz and clays and feldspars have weak statistical significance.

noneolian material (Krissek and Clemens, 1991) may be a necessary step in order to achieve similar results.

3.6 Discussion

The data gathered from the QEMSCAN® instrument on grain-size (Figure 3.3) shows similar results to earlier work (Clemens and Prell, 1991). This suggests that QEMSCAN® is a reliable rapid reconnaissance instrument for grain-size research involving deep-sea sediments. With this in mind, some discussion of what these grain-size data reveal about paleoclimate is warranted.

Grain-size peaks are found in the dolomite/quartz average at 27 ka, 51 ka, 69 ka, 81-100 ka, 130 ka, 145 ka, 159 ka, and 174 ka aged core horizons from ODP Hole 722B. Some of these peaks, specifically 27 ka, 51 ka, 69 ka, 81 ka, and 91 ka coincide with, or occur at nearly the same time, as known glacial millennial climate (GMC) events (Table 3.2). These events include Dansgaard-Oeschger (DO) events, and Heinrich (H) events, which appear to be linked to small changes in solar insolation.

Table 3.2

Glacial Millennial Climate Events and Grain-Size

Grain-Size Peak Age (ka)	GMC Events	GMC Event Ages (ka)
27	DO-2; H-2	26-23; 26-24
51	DO-13; H-5	52-50; 49-47
69	DO-18	69-65
81	DO-20?	78-77
91	DO-22	97-90

Dansgaard-Oeschger events are defined by sharp spikes in the Greenland ice core $\delta^{18}O$ record, and represent brief warming periods during glacial intervals, of up to 15° C, that last 500-2500 years (Dansgaard et al., 1984; Oeschger et al., 1984; Dansgaard et al., 1993). These periods of warming are usually preceded by Heinrich events. Heinrich events are brief periods of sediment deposition via ice-rafting (Heinrich, 1988) and subsequent ocean surface cooling over large parts of the North Atlantic Ocean (Bond et al., 1992; Andrews et al., 1998; Hemming 2004; Cronin, 2010). This "flip-flop" of climate state in the North Atlantic appears to affect the Tropics, including the East Asian Monsoon, although whether the source of climate change originates in the Tropics or the North Atlantic is still debatable (Broecker, 2003).

The East Asian Monsoon has been linked to North Atlantic climate via millennial scale events (Broecker, 1994; Hughen et al., 2000; Kienast et al., 2001; Wang et al., 2001; Burns et al., 2003). The oxygen-isotope record captured in speleothems in the Indian Ocean region shows that DO events caused the climate to become quite dry, prior to the warming that led to wetter conditions (Burns et al., 2003). Such an increase in drying prior to a wetter climate would have created increased dust potential for the surrounding region (Goudie, 1983; Prospero et al., 1989), and the subsequent increased warming and wetness following would have temporarily strengthened monsoon winds. Such conditions lead to larger grains being carried by stronger monsoon winds, and a temporary increase in grain-size is observed. This appears to point to solar insolation variance strongly affecting the grain-size record through time, with the earlier grain-size peaks perhaps being related to similar glacial millennial events.

In contrast to the grain-size data, the mineralogical data from QEMSCAN® shows very little correlation to previous work (Krissek and Clemens, 1991). Although dolomite percentage correlates well with the relative abundance calculated by Krissek and Clemens (1991), the clays

and feldspars and quartz percentages and abundances do not. The reason for the lack of correlation is currently unresolved, but is likely due to differences in sample preparation or sample quality. This is also confusing, as QEMSCAN® reliably detects quartz, and the SIP used excels at doing so. The differences for quartz may be explained by the unique ability of QEMSCAN® to analyze samples without the need to remove biogenic carbonate and other organic material. As such, samples for this study are in-situ, and have not been disturbed by chemical treatment. It is also a possibility that the portion of sample received for this study was different from the sample used by Krissek and Clemens (1991), as the core is quite depleted at this time. Regardless of the cause of data discrepancy, the data do show that dolomite and quartz grain-size increases during GMC events. Another unexpected result is that dolomite grain-size does not consistently correlate to increases in dolomite abundance as one might expect. However, the data do show that clays are somewhat inversely correlated to dolomite and quartz, showing that processes behind depositional factors do differ based on regional climate as suggested by Krissek and Clemens (1991).

3.7 Conclusions and Future Work

Grain-size research using QEMSCAN® is better than previous methodologies when looking at individual minerals. The reliability of data collected by the instrument, and high resolution of important eolian minerals, points to a new paradigm in grain-size paleoclimate research. The implications of dolomite and grain-size being much smaller than earlier studies, yet still telling similar paleoclimatological stories, suggests that some estimations of monsoon paleowind strength may need to be reevaluated. Mineralogical analysis on the other hand is uncertain. Although QEMSCAN® measurements for dolomite area percent correlate well with

earlier work, the weak correlation to quartz and clays and feldspars implies an unknown variable in the data. However, it should be noted that QEMSCAN® is being used as a "micro" technique in this study, focusing on only a few minerals. Bulk analysis using XRD does not do this, meaning that the differences could be explained solely due to methodological differences.

Future work using QEMSCAN® requires, first and foremost, a SIP calibrated and tailored for the region's sediment. With such a SIP, more samples from ODP Hole 722B should be analyzed and investigated for paleoclimatological patterns. Such research could help resolve the cause of grain-size change, and the enhanced SIP would allow for better mineralogical analysis.

QEMSCAN® would also allow for determination of whether grain-size changes are due to provenance changes or changing monsoon wind strengths. Some evidence for this is seen in the dolomite and quartz median grain-size data. At several instances, dolomite, the denser mineral, has larger grain-size than quartz, which is less dense. With more data and samples, this could point to monsoon wind strength being the primary control on grain-size, with dolomite coming from the Arabian Peninsula, and quartz from possibly a different quarter.

Paleoclimatological precursor events to DO and H events should also be sought out in the Arabian region. The rapidity of QEMSCAN® analysis is ideal for mineralogical precursor events, and could possibly help determine if the source of global millennial shifts originates in the North Atlantic, or in the Tropics, which react violently to such events. In summary, what are needed are more samples to increase data density, samples from less depleted portions of core, and better calibrated instrumentation and methodology.

CHAPTER 4

XRF ANALYSIS OF LL44-GPC3 CORE, CENTRAL NORTHEAST PACIFIC

As Earth orbits around its star Sol, there is a high probability that it may collide with any number of near Earth objects. Any such impact by a bolide would be disastrous, as modern civilization is vulnerable to such events (Pierazzo and Artemieva, 2012). Understanding the environmental effects of such catastrophic geologic events allows humanity to better prepare for when they will happen. However, in order to understand such effects, a key piece of evidence is needed. That evidence lies, in part, with the distribution of debris after impact. These debris fields, known as strewn fields, are littered with glassy ejecta called tektites, some of which are rich in nickel, an element not common in Earth's crust, but common in meteorites (Pierrard et al., 1999). Some tektites are known as microkrystites (Pierrard et al., 1999; Vonhof and Smit, 1999), and are essentially nickel-rich spinel. Being able to rapidly identify core horizons rich in nickel-rich spinel, and therefore extraterrestrial matter, would be a benefit to researchers searching for bolide impact tracers. It is posited that using handheld X-ray fluorescence (XRF) instruments allows for such rapid reconnaissance, and is a viable detector of nickel-rich core horizons in deep-sea sediments.

4.1 Depositional Setting

The LL44-GPC3 core is located in the Central Northeast Pacific Ocean (Figure 4.1) at 30° 19.4' N, 157° 49.4' W, in 5705 m of water (Janacek and Rea, 1983). The core consists of yellow-brown lutite, or "red clay," in the upper portion (0-632 cm), and dark brown lutite in the lower portion (632-2432 cm), and is a mixture of eolian debris, authigenic hydrogenous material, and phosphatic biogenic sediment (Corliss and Hollister, 1979). The location of the core places it away from sources of biogenic, hydrothermal, ice-rafted, and turbidity-current sediments (Leinen and Heath, 1981), and in an area of low energy bottom circulation (Taft et al., 1981), minimizing erosion and redeposition processes. However, the core is significantly burrowed, meaning that it is likely that any extraterrestrial events may well have been smoothed out over as much as 10 cm vertically. The core is unique, in that it contains a continuous Cenozoic section (Doyle and

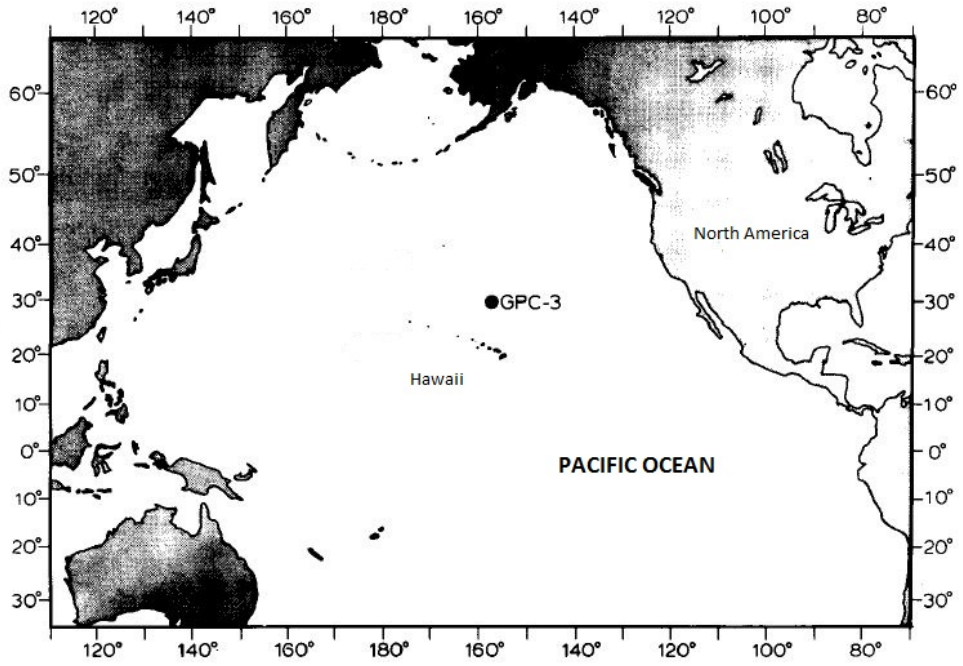

Figure 4.1. Location of LL44-GPC3 core. Modified from Vonhof and Smit (1999).

Riedel, 1979), which continues back to the Cretaceous, that has been well-dated by paleomagnetic reversals (Prince et al., 1980) and ichthyolith stratigraphy (Doyle and Riedel, 1979; Doyle, 1980).

4.1.1 Nickel Distribution in the North Pacific

Nickel is rare in the Earth's crust, and its distribution in North Pacific sediments has little reason to vary much from ~293 ppm (Chester, 1965; Chester and Hughes, 1966). How this nickel is incorporated into the deep sea sediments has been the subject of much controversy (Goldberg, 1954; Laevastu and Mellis, 1955; Pettersson, 1959; Landergren, 1964). Regardless of how the nickel got to the ocean, the concentration appears to be fairly consistent, with little variation, throughout the Pacific Ocean (Chester and Hughes, 1966), and is usually associated with hydrothermal activity and precipitation from seawater (Dymond et al., 1973).

4.2 Previous Work

Evidence for up to three bolide impacts during the late Eocene to Early Oligocene is found throughout the world, in the form of microtektites/microkrystites (Pierrard et al., 1999), shocked quartz (Clymer et al., 1996), high iridium (Montanaria et al., 1993), and high ^{3}He concentrations (Farley et al., 1998). These findings support those of Pierrard et al. (1998), which found nickel-rich spinel crystals at the Eocene/Oligocene boundary at Massignano, Italy. The layer in which the nickel-rich spinel is found also contains high amounts of iridium and shocked quartz (Pierrard et al., 1999), key indicators of bolide impacts.

To determine if these impacts are recorded elsewhere in the world, Pierrard et al. (1999) investigated various deep-sea cores, including ODP Hole 689B, DSDP Site 94, DSDP Site 612,

and LL44-GPC3. At ODP Hole 689B, Maud Rise, Southern Ocean, both Pierrard et al. (1999) and Vonhof and Smit (1999) found nickel-rich spinel crystals in a 20 cm-thick layer containing iridium, microkrystites, and microtektites, coinciding with the impact horizon at Massignano. The same features are observed at DSDP Site 94, Gulf of Mexico, with nickel-rich microkrystites, and at DSDP Site 612, US East Coast, with iridium, microkrystites, and microtektites (Pierrard et al., 1999). In the giant piston core LL44-GPC3 from the Central North Pacific, Ocean Pierrard et al. (1999) found two nickel-rich spinel peaks at 11.1 meters and 12.4 meters depth below seafloor. Overall, these findings and geochemical research done by Vonhof and Smit (1999) suggest three bolide/cometary impacts near the Eocene/Oligocene boundary.

4.3 XRF Analysis Results

The LL44-GPC3 core samples provide substantial amounts of elemental peak counts for each element. As nickel-rich spinel is found at 11.1 m and 12.4 m depth (Pierrard et al., 1999), samples investigated for this study are clustered around these points. Other horizons from throughout the core are also measured to determine the average nickel peak count. The average nickel peak intensity counts for the core are ~ 2500 including the highs.

Sections of core with nickel counts exceeding background nickel values were selected for closer study after tabulation (Table 4.1). The highest nickel peak counts cluster around the core horizons at 11.1 m and 12.4 m depth (Figure 4.2), in the intervals 11.0-11.2 m and 12.0-12.5 m. Two high nickel peak count outliers, at depths of 9.3 m and 18.68 m, are also present. However, as sampling is focused around the 11.1 m and 12.4 m depths with nickel-rich spinel described by Pierrard et al. (1999), there is no way to determine if high nickel observed at 9.3 m and 18.68 m are indicative of impact events, or outliers within the data.

Table 4.1

XRF Elemental Peak Counts

Depth (m)	[a]Al	Ca	Cl	Cu	Fe	K	Mn	Ni	P	S	Si	Ti	Zn
0.73	18419	12073	43861	6656	925345	54263	50814	1001	1	913	92915	35501	2238
4.6	18113	14801	36603	7458	978054	54486	85574	1723	1	614	90493	39473	2057
5.1	17583	15417	46097	8177	990127	54052	103014	2090	13	700	91273	39467	2468
5.7	17373	15877	45663	7111	958539	54827	79655	1110	1	789	89166	38056	2044
6.3	16832	14744	48567	7086	981540	51513	50379	978	1	1328	85269	38896	2138
7	15054	20553	41255	7959	1022786	47428	115324	1091	1	918	79388	42392	2029
7.4	15734	21944	57044	7896	973142	46758	121259	1759	0	1184	83171	40747	2095
9.3	12944	40580	64766	7584	799699	36658	232212	3788	832	1259	71410	34814	1375
10.1	12119	36519	65417	4167	671956	34919	215261	2014	1168	1432	63035	26259	966
11	13856	41057	69743	7273	967607	45467	295860	3054	1099	2090	73270	26617	1758
11.1	15126	32999	47485	7001	945795	57227	282818	2543	746	1436	75995	25153	1944
11.2	14089	38344	69638	6870	964896	46246	331572	3524	1033	1544	72588	23739	2013
12	14474	45461	70896	6530	844686	46245	285535	4486	1544	1299	78488	23210	1737
12.3	11807	41255	67723	5875	815371	38773	299892	4516	1504	1466	63040	17994	1991
12.4	12065	50427	54593	6820	882049	39497	331945	5254	2561	1315	66673	18673	1829
12.5	11847	46885	55961	6806	911610	37095	347624	5237	2020	957	64039	19255	2219
13.1	14738	21962	58204	6923	737703	40027	129493	2234	234	1459	73451	13682	1846
14.9	8249	43653	65357	7131	1376749	28066	352568	2069	2099	1253	48104	16439	2445
15.9	8072	60849	71968	6476	1126538	26862	376749	2437	3532	1627	49551	16448	1818
16.7	6394	88009	71109	8981	1453452	16213	301399	1361	5971	1403	38909	11473	1943
17.2	7386	111754	46791	8952	1227080	25319	305742	2131	8837	907	47332	13437	2359
18.68	10594	83447	75900	11157	962823	38442	251185	3034	4736	1654	71828	13188	2677
20.88	11482	31915	70285	10890	869012	30218	204454	1743	812	1109	75477	14834	3882
23.75	12581	33205	61273	8000	985304	47327	178576	2218	1277	1102	78102	20880	2387

[a]Elemental peak counts are for Aluminum (Al), Calcium (Ca), Chlorite (Cl), Copper (Cu), Iron (Fe), Potassium (K), Manganese (Mn), Nickel (Ni), Phosphorous (P), Sulfur (S), Silicon (Si), Titanium (Ti), and Zinc (Zn).

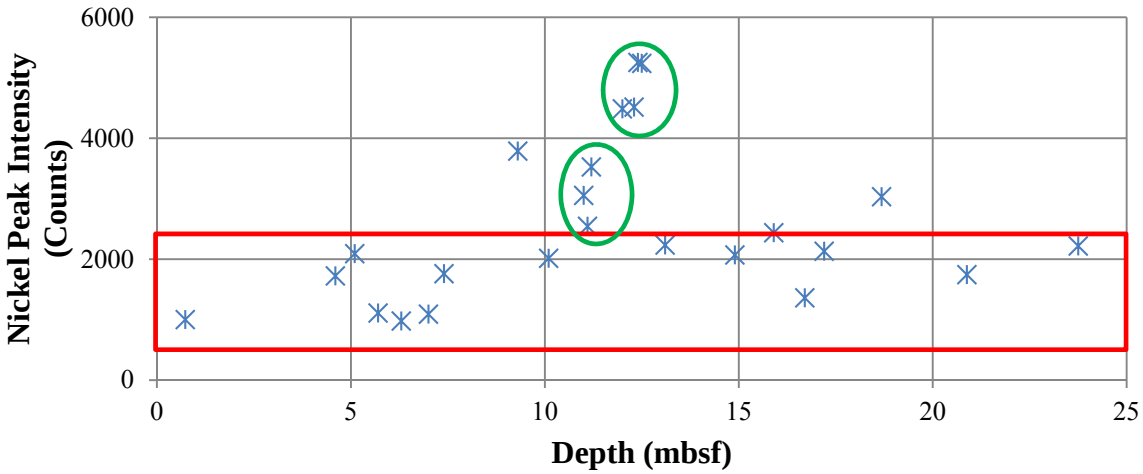

Figure 4.2. Peak nickel intensity counts plotted as a function of depth. Red rectangle outlines the average background nickel for the LL44-GPC3 core, and green ovals circle high nickel peak count clusters at 11.1 and 12.4 mbsf. Note also the high nickel counts at 9.3 and 18.68 mbsf.

4.4 Discussion

The first noticeable pattern in the data is that the average nickel counts detected by the handheld XRF are ~ 2500, which is rarely exceeded in any core horizon (Figure 4.2). This is consistent with nickel having a stable background concentration (Chester, 1965; Chester and Hughes, 1966) in the Pacific Ocean. However, two clusters of points at 11.1 m and 12.4 m depth below seafloor are present, and match the core horizons where nickel-rich spinel crystals are found (Pierrard et al., 1999). As background nickel is usually derived from hydrothermal activity and precipitation from seawater (Chester and Hughes, 1966; Dymond et al., 1973), these increases cannot be explained away as such. An explanation for the unusual spikes in nickel is provided by the ichthyolith dates of these sediments (Doyle and Riedel, 1979; Doyle, 1980), being from the late Eocene (12.4 m) and early Oligocene (11.1 m). These dates correlate well with other impact horizon evidence (Montanaria et al., 1993; Clymer et al., 1996; Farley et al.,

1998; Pierrard et al., 1998; Pierrard et al., 1999; Vonhof and Smit, 1999), and suggest that the peaks represent the same impact events.

4.5 Conclusions and Future Work

The data clearly show that handheld XRF successfully identified two points of interest in the LL44-GPC3 core. Although the data are preliminary, the correlation with previous work (Pierrard et al., 1999; Vonhof and Smit, 1999) links the nickel peaks with the Chesapeake Bay and Popigai, Siberia impact events. The two single points above the nickel count average from 9.3 m and 18.68 m depth may represent impact events as well; however, no correlation to known impacts is available, and the nickel count at 18.68 m is only slightly above the background level. Regardless, the data illustrate the possibility of using handheld XRF as a rapid reconnaissance technique in investigating deep-sea sediments for impact horizons using nickel as a tracer element.

As XRF is routinely used in logging core investigations, an average background nickel concentration for the Pacific Ocean can and should be established. This would make using anomalously high nickel as a tracer for impact events much more refined. The high nickel counts found at 9.3 m and 18.68 m also warrant further investigation, and correlation to impact evidence determined. Further investigation of the LL44-GPC3 core via QEMSCAN® is also a distinct possibility, as the instrument may be able to detect extraterrestrial material. However, our reconnaissance QEMSCAN® study of a sample from 12.4 m, not reported here, failed to detect any evidence of microkrystites: all particles with high nickel counts also had substantial manganese, consistent with manganese precipitate but not with nickel spinel. This may be due to the inability of QEMSCAN® to distinguish between the fine geochemical differences of

ferromanganese nodules and microkrystites. This issue may be resolved by creating a SIP designed solely to investigate trace components in deep-sea sediments such as manganese and nickel. Ultimately however, due to the rarity of extraterrestrial tracers in deep-sea sediments, success rates for such research may be dismal and doomed to failure.

CHAPTER 5

CARBONATE CEMENTATION EFFECTS ON VELOCITY, CANTERBURY BASIN, OFFSHORE NEW ZEALAND

Most changes in compressional-wave velocity in siliciclastic sediments are attributable to changes in porosity, fitting accepted compaction trend models (Wyllie et al., 1956; Stoll, 1989; Erickson and Jarrard, 1998; Jarrard et al., 2000). However, when sediment velocity increases much more than expected based on such models, another explanation is needed. The effects of cementation on velocity provide such an explanation (Jarrard et al., 2000).

Chemical compaction is a diagenetic process, and as such requires conditions appropriate for chemical reactions to occur. For carbonate precipitation from fluid flow and subsequent cementation, temperatures need not be high. Rather, the diagenetic reaction can occur at any location where appropriate porosity and fluid flow occurs in siliciclastic sediments. Mechanical compaction decreases sand porosity only gradually with depth (Taylor, 1950), whereas clay porosity decreases more rapidly due to their “cardhouse” fabric (Magara, 1980) collapsing into parallel arrangements. As a consequence, the permeability of clay-rich muds is reduced much more than that of sands. This allows fluid flow to occur mainly within sandy sediments, and carbonate-rich waters to precipitate calcite into the pore space of sandy sediments. This

cementation increases the velocity of sands and sandstones partly by decreasing porosity, but mainly by increasing framework modulus (Jarrard et al., 2000).

Brusova (2010) found sandy sediments from IODP Leg 317 to have higher than expected velocities, and to be much faster than the velocities of adjacent shales. This effect was hypothesized to be due to carbonate cementation, but as yet has not been demonstrated. As calcium, the primary component of calcite, is an element easily detected using handheld XRF, it is posited that calcite can be tracked in siliciclastic sediments, and can be linked to the sandy sediments. Such data would persuasively show that calcite cementation in Canterbury Basin sediment can be linked to the higher than expected compressional-wave velocities observed in those sediments.

5.1 Depositional Setting

The Canterbury Basin is located on the eastern margin of New Zealand's South Island (Figure 5.1), and is part of the Eastern New Zealand Oceanic Sedimentary System (Carter et al., 1996). The region is bounded by two volcanic centers, the Banks Peninsula on the northeast, and the Otago Peninsula to the southwest. Sediments within the basin thin towards these features, as well as towards the shore, where they overlie basement rock involved in the uplift of the Southern Alps (Adams, 1979; Tippett and Kamp, 1993a; Batt et al., 2000).

The basin is the landward edge of a continental fragment rifted from Antarctica ~80 Ma, which underlies the present-day onshore Canterbury Plains and offshore continental shelf (Field and Browne, 1989). Rifting continued via a mid-ocean-ridge in the southern Tasman Sea and Pacific, with the Canterbury Basin as a passive continental margin. During the Oligocene, ramplike sediment geometries (Fleming, 1962) and calcareous biopelagites were deposited

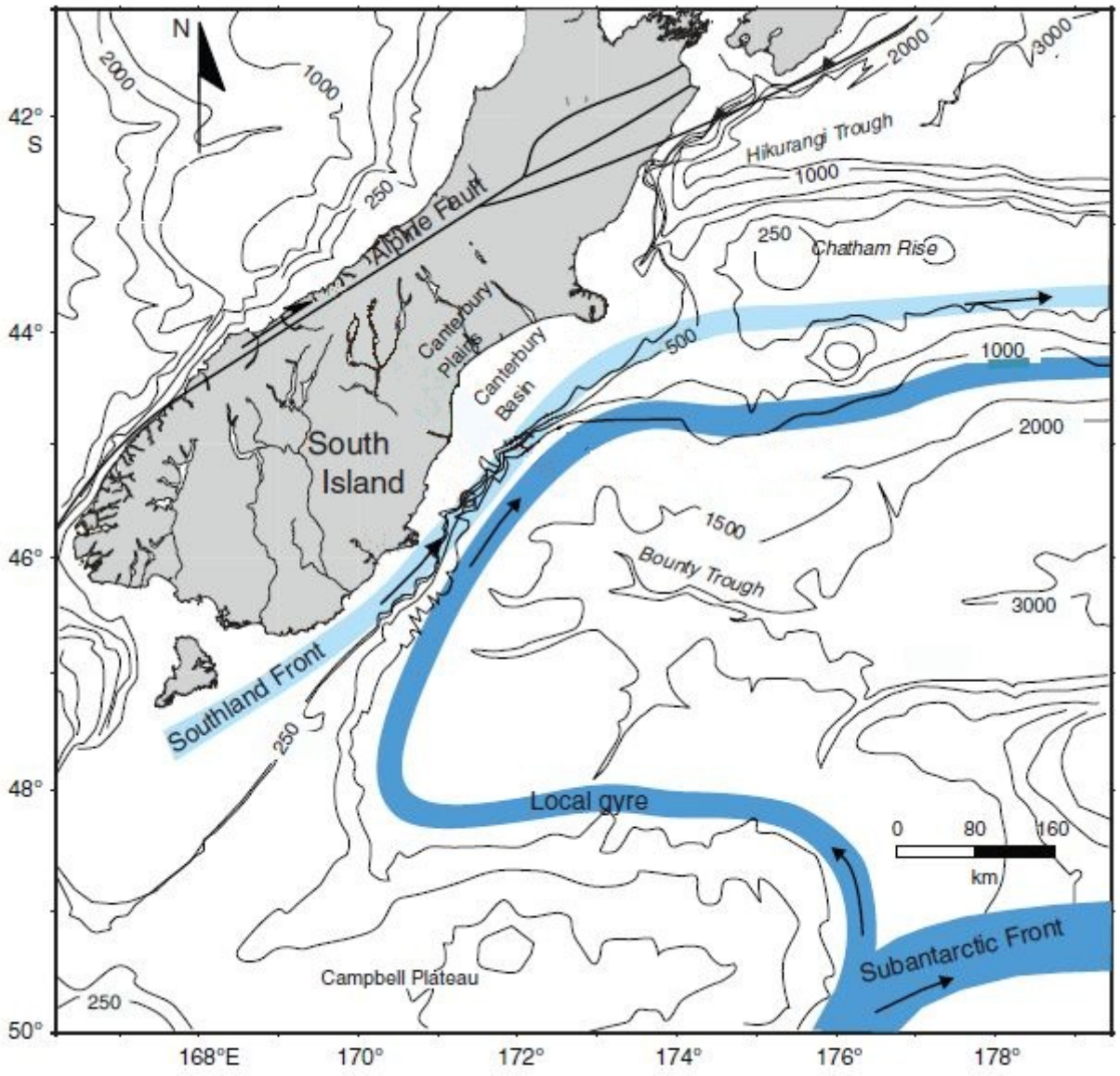

Figure 5.1. Location of the Canterbury Basin. Map shows associated faults, currents, and bathymetry. Modified from Expedition 317 Scientists (2011).

(Expedition 317 Scientists, 2011). At ~ 55 Ma, the Indian Ocean and Pacific spreading centers linked together, curtailing the Tasman Sea mid-ocean-ridge spreading by the late Eocene (Expedition 317 Scientists, 2011). This new continuous Indian-Pacific Southern Ocean ridge system led to the development of the modern Australian-Pacific plate boundaries (Molnar et al., 1975), including the Alpine fault ~23 Ma in the early Miocene (Wellman, 1971; King, 2000). The current orogenic activity of the Southern Alps was enhanced ~10-5 Ma (Carter and Norris, 1976; Norris et al., 1978; Adams, 1979, Tippet and Kamp, 1993a; Tippet and Kamp, 1993b; Batt et al., 2000) due to increasing convergence along the plate boundary, leading to an increase in sediment supply to the Canterbury Basin (Lu et al., 2005). This has led to the Canterbury Basin having a high Neogene sediment supply (Fulthorpe and Carter, 1989), which continues to the present. Such sediment deposits have been termed "Canterbury Drifts" (Carter, 2007), and have been heavily influenced by the Southland Current, a local gyre of the Antarctic Circumpolar Current (Morris et al., 2001).

5.2 Previous Work

IODP Expedition 317 set out to investigate global sea level, or eustasy, controls, versus local tectonic and sedimentary controls on continental margin sedimentary cycles (Expedition 317 Scientists, 2011). In order to accomplish this objective, four sites were cored in transect from landward to continental slope through the basin, U1353, U1354, U1351, and U1352. Ages and lithology were documented (Figure 5.2). Within these sediments, carbonate content increases with depth, especially at Site U1352 (Expedition 317 Scientists, 2011).

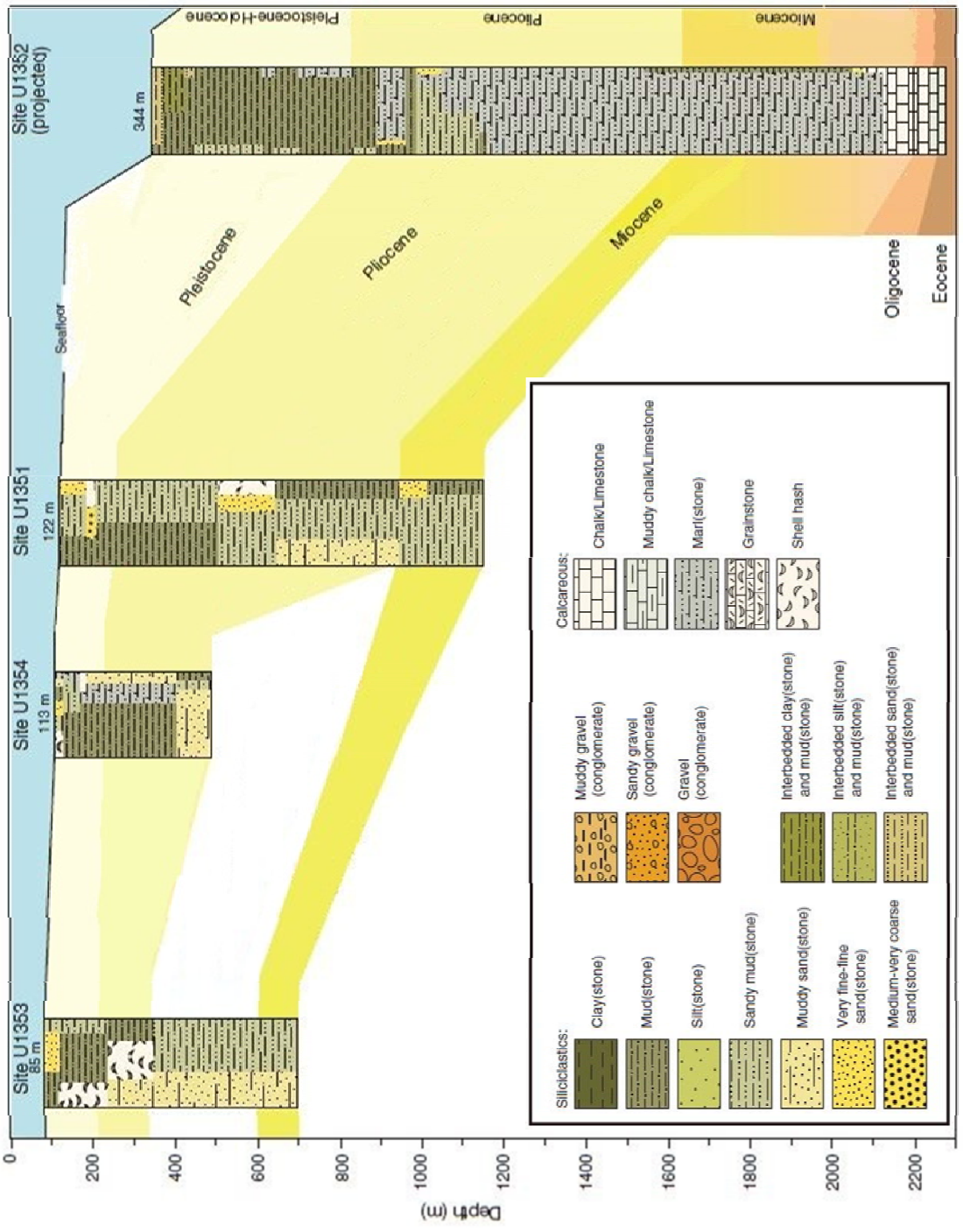

Figure 5.2. Sites and relative ages of IODP Leg 317. Modified from Fulthorpe et al. (2011).

Brusova (2010) investigated porosity and velocity compaction trends of the three primary lithologies in the Canterbury Basin. This included sand, silt, and shale, but not lithologies in low concentrations, such as coal and limestone (Brusova, 2010). These data show that sand, silt, and shale velocities all increase with depth. Of these, sand has the highest velocity increase of the siliciclastic sediments (Figure 5.3). According to Brusova (2010), the velocity trends for the lithologies in the Canterbury Basin are less representative for beds with different cementation patterns. This is especially true for Canterbury Basin sandstones, which have high velocities often, likely due to many sands being somewhat carbonate cemented (Brusova, 2010).

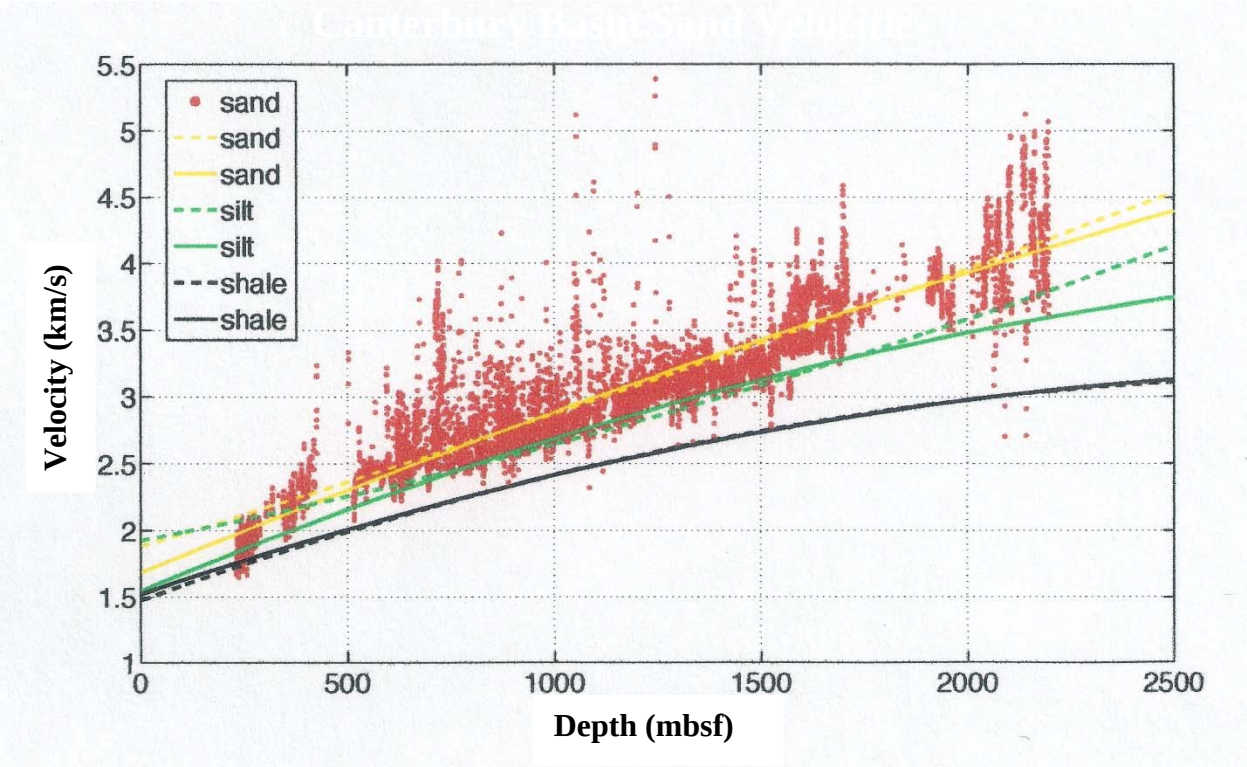

Figure 5.3. Canterbury Basin sand velocities as a function of depth. Comparisons made to local velocity curves for sand, silt, and shale. Note how high sand velocities are compared to silt or shale. Modified from Brusova (2010).

5.3 XRF and Velocimeter Analyses Results

Elemental data collected by the handheld XRF shows inverse and positive correlations. Such relationships can be used to reveal what elements are present in sands and clays. The element silica (Si) would seem to be a logical starting point for this type of investigation as it is the primary component of quartz sands (SiO_2). However, Si being present in both clays and sands precludes it. Instead, the element iron (Fe), an essential component of clays (Carroll, 1958), is used as a proxy for clay minerals in this study. To substantiate that Fe is a clay proxy for Canterbury Basin sediments, the elements manganese (Mn), potassium (K), and titanium (Ti), common in many clay minerals (Mermut and Cano, 2001), are investigated, and correlated to Fe as well.

Mn is found to increase with Fe, indicating that it is found within the same lithologies (Figure 5.4a). This same correlation is observed for both K (Figure 5.4b) and Ti (Figure 5.4c): both elements covary with Fe. These results suggest that Fe, Mn, K, and Ti are present within the same component, clays, within the Canterbury Basin. This is further strengthened by all elements having a strong positive correlation lying well within the > 99 % confidence level (Fisher and Yates, 1948), with Mn, K, and Ti having R values of 0.9449, 0.9220, and 0.9608, respectively. These are near perfect correlation coefficients, as the value 1.0000 is perfect.

Peak intensities for both iron and calcium collected by the XRF are then compared to determine whether cementation is concentrated in the sands or clays of the Canterbury Basin. Iron and calcium have an inverse relationship (Figure 5.5), with calcium being low in sediments with high iron, and high in sediments with low iron. This observation demonstrates that carbonate cementation is concentrated in sandy sediments from the Canterbury Basin, and not within muds, and the inverse correlation lies within the > 99 % confidence level.

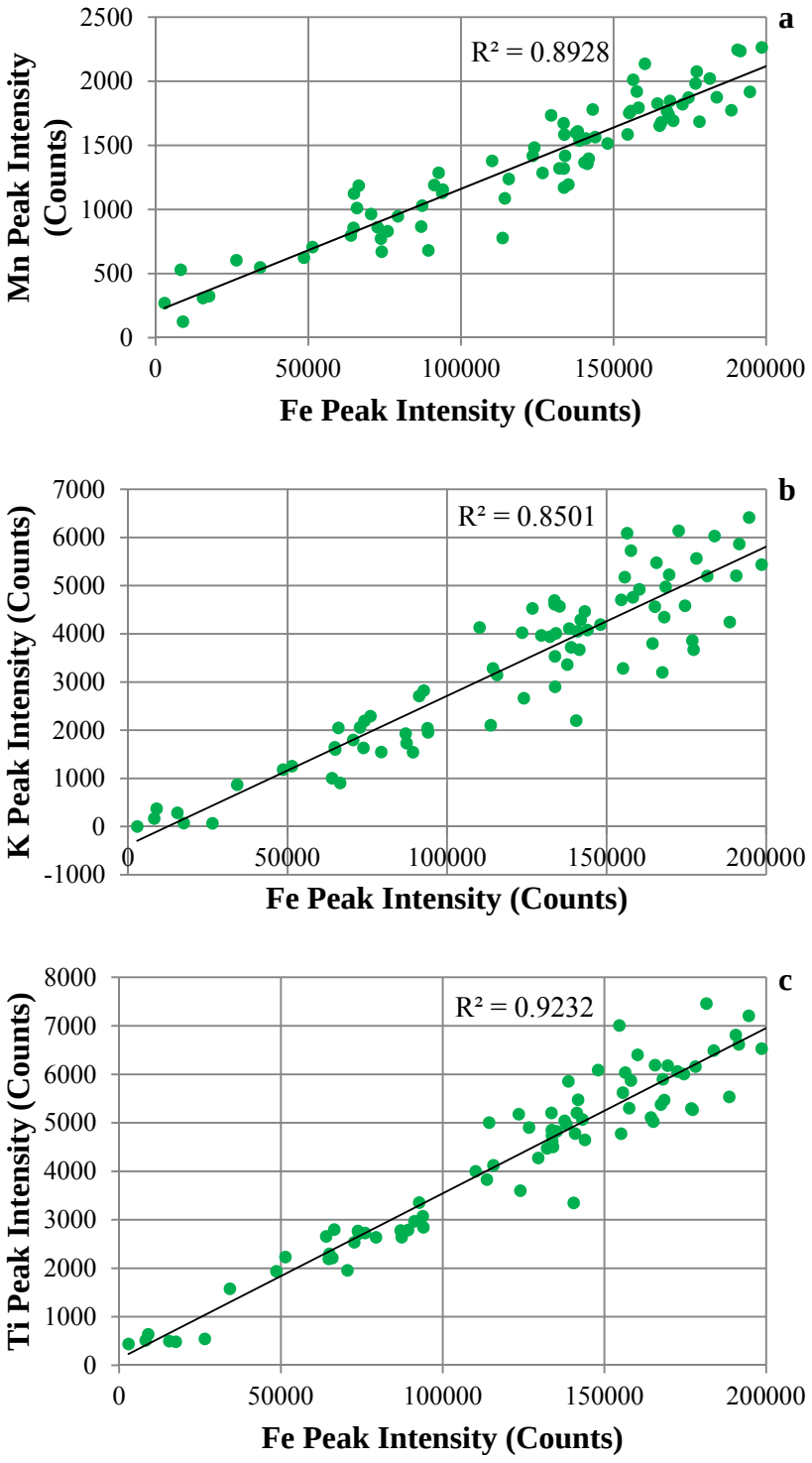

Figure 5.4. Peak counts for common clay elements. Note the common clay element iron's peak counts versus other elements found in clays: **a** is manganese, **b** is potassium, and **c** is titanium. All have a > 99 % confidence level for significance of the correlation coefficient, showing strong positive correlation for Fe, Mn, K, and Ti. This suggests Fe to be a valid proxy for clays.

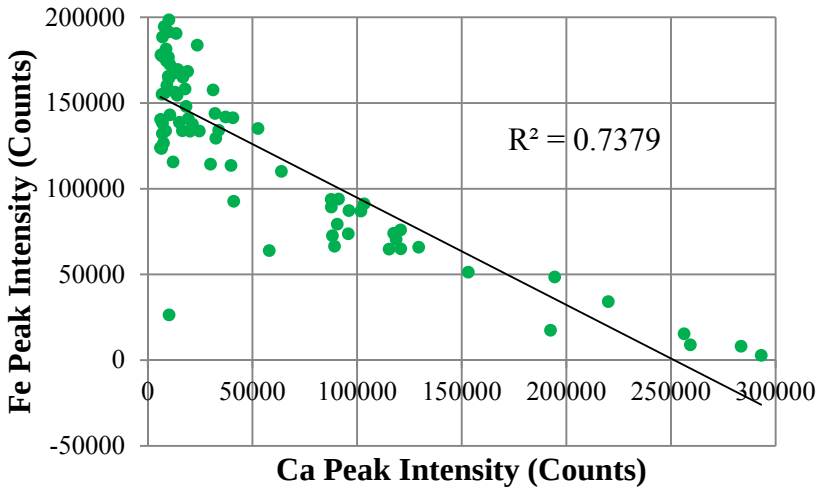

Figure 5.5. Inverse relationship of calcium and iron in the Canterbury Basin. This relationship shows that calcite precipitation is concentrated in the sediments with lowest clay content, and is within the > 99 % confidence level for statistical significance.

With calcite effects present in sands, not clays, the effects of calcite on velocity can now be examined. P-wave velocities are compared to the calcium peak intensity counts in each sample from the Canterbury Basin used in this study. With calcium now known to be a valid proxy for sand (Figure 5.5), the data should show that increasing calcite correlates with increasing velocities. Such comparison of calcium counts against velocity does show that as the calcium content increases, so does the compressional-wave velocity of sediments (Figure 5.6) with correlation in the > 99% confidence level (Fisher and Yates, 1948) with a correlation coefficient of 0.8588. This is consistent with the previous work done by Brusova (2010), and suggests that calcite cementation is greatly affecting the velocities of sandy sediments in the Canterbury Basin. However, the correlation of calcium counts and velocity may be partially indirect, caused by both calcite and compaction increasing with depth as carbonate sediments increase downcore.

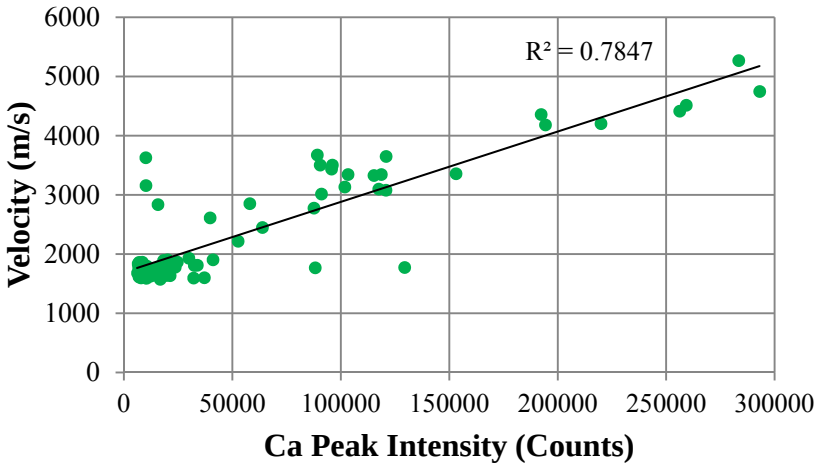

Figure 5.6. Calcium's effects on velocity in Canterbury Basin sediments. Note that as calcium increases, so does the velocity of sediment. Confidence level is > 99 % for correlation.

5.4 Discussion

To separate the effect of depth-dependent compaction and calcite cementation, the samples are divided into two groups: low-calcium and high-calcium. For this study, > 65000 peak counts from the handheld XRF are high-calcium, as it is the first significant increase noted in the data (Appendix). When these data are compared to the velocity and depth measurements for each sample, two distinct populations can be seen (Figure 5.7). The low-calcium peak count sediments (red) are, for the most part, at shallow depths above 1000 mbsf. The high-calcium-bearing sediments (green) are present from ~700 mbsf and deeper in the drillholes. Within the top 700 mbsf, none of the samples have high calcium, whereas all of those below 1500 mbsf do. The source of this calcium appears to related to the deep carbonate layers within the lithology (Figure 5.2).

The velocity measurements of the high-calcium core horizons are characterized by having velocities that exceed 2500 m/s, with the exception of two samples. This contrasts with most of the low-calcium sediments, which increase in velocity only by ~500 m/s, even at 1000

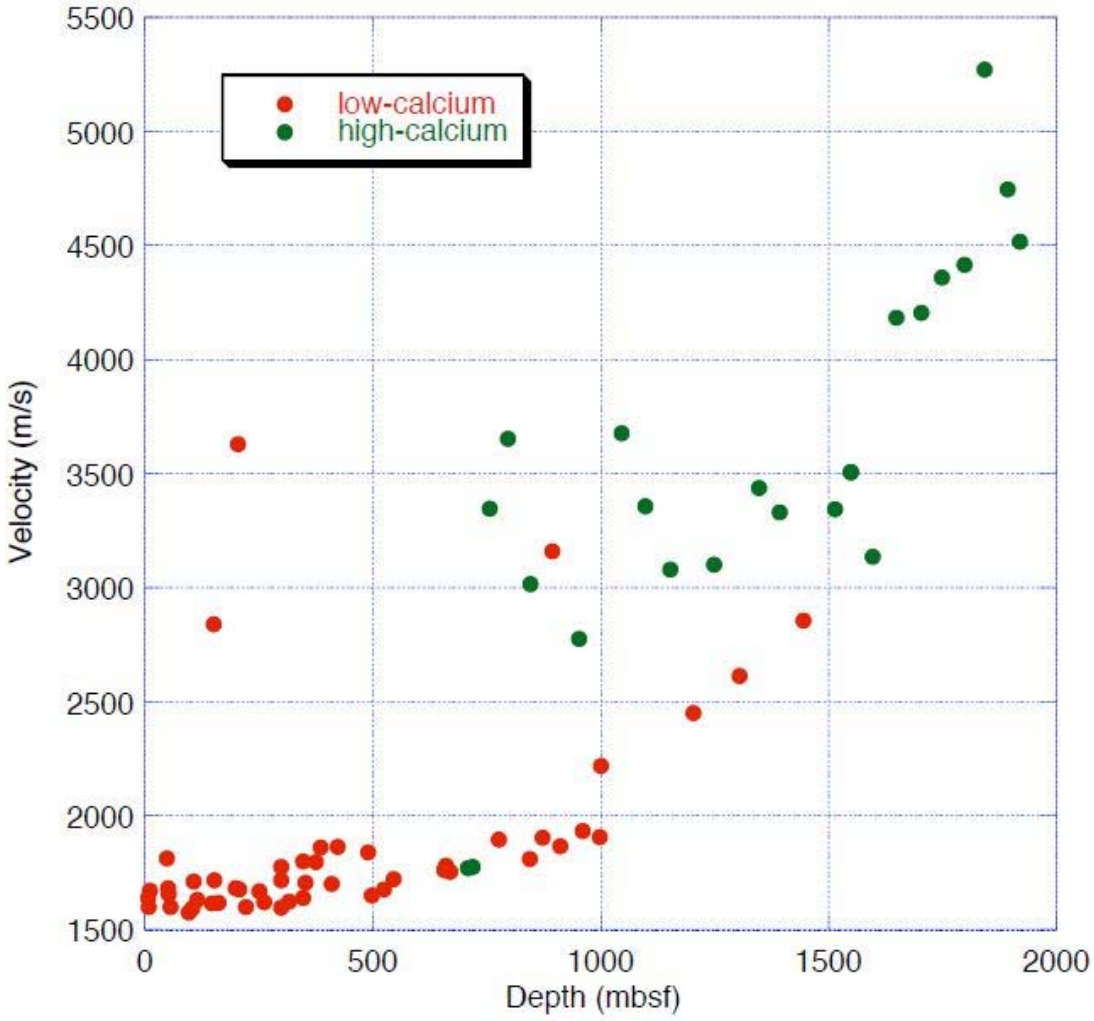

Figure 5.7. Low- and high-calcium in Canterbury Basin correlated with depth and velocity. Low-calcium occurs at shallow depths and has low velocity, while deeper sediments contain high-calcium and have high velocities.

mbsf. The high-calcium sediments, however, increase 1000-2000 m/s over approximately the same depth.

Such velocity changes cannot be simply explained away via mechanical compaction, although that is certainly happening as observed by velocity increasing with depth in both high- and low-calcium sediment populations. Rather, another process is acting upon these sediments. In the depth interval 750-1500 m, where carbonate cementation is highly variable (Figure 5.7), cementation clearly causes a major increase in velocity. This is in agreement with Brusova's (2010) speculation that carbonate precipitation may increase sand velocities in the Canterbury Basin, and with the similar conclusion by Jarrard et al. (2000) for Antarctic sediments. However, neither of those studies paired velocity and calcite analyses, as this study does.

5.5 Conclusions and Future Work

Calcite diagenesis does indeed have a profound impact on Canterbury Basin sediments. The confirmation that the cementation effect is occurring primarily in sands and not in clays points to calcite being sourced from deeper carbonate-rich limestones. As the sandstones in the basin are high porosity (Expedition 317 Scientists, 2011) in a tectonically active region, this comes as no surprise. However, what is surprising is how much of an impact carbonate cementation has on observed compressional-wave velocities in the siliciclastic rocks. For example, if these sediments were unconsolidated sediment without cementation, the velocity would be expected to be much lower than that observed. As observed velocity increases coincide with sands and high calcite content, the data appear to show direct evidence of carbonate cementation increasing compressional-wave velocity in siliciclastic sediments.

Not only do the data illustrate cementation and its effect on sediment velocities, they also demonstrate the effectiveness of using handheld XRF in deep-sea sediment investigations in which geochemical data are useful. For example, in conjunction with velocity measurements, causes of significant increases in velocity have been determined to be due to cementation of sandy sediments. This information was garnered rapidly by using handheld XRF reconnaissance as an efficient nondestructive methodology useful for small amounts of sample. This suggests that the same methods can be used in future work to investigate other unexplained velocity increases in sediments from cores with little sample remaining for study.

Future work can take two different directions. The handheld XRF can be used to improve compaction trend models by providing ground truthing for velocity increases in a given sediment column. Brusova (2010) effectively determined compaction trends for velocity and porosity for Canterbury Basin sediments, and her data can be used as a starting point for such research. Also of interest would be comparing the gathered Canterbury Basin elemental data to porosity data. If calcium velocity increases could be tied to low porosity sediments, it would further support the conclusion that high-calcium cementation occurs in sandy sediments.

APPENDIX

XRF AND VELOCIMETER DATA FROM THE CANTERBURY BASIN, NEW ZEALAND

Table A.1

Canterbury Basin XRF Peak Count Data

Sample ID	Al	Ca	Cl	Fe	K	Mn	S	Si	Ti
1351b-2h-5-69-72	1083	40656	12392	141496	3673	1357	506	1326	5205
1351b-8h-1-117-119	1334	33809	21964	134133	4012	1419	686	3326	4505
1351b-16x-2-55-57	1049	12480	19777	167493	3201	1768	550	781	5379
1351b-21x-1-117-119	1087	6992	21342	177264	3673	2077	459	754	5269
1351b-27x-2-102-105	1039	7841	13774	155717	5179	1768	323	896	5623
1351b-31x-4-24-26	1081	6953	15219	188630	4244	1774	473	728	5536
1351b-37x-2-51-53	1065	8886	17089	174586	4583	1874	384	682	6005
1351b-41-1-70-73	1072	9977	19272	164404	3799	1827	464	738	5110
1351b-47-1-25-28	997	13934	12915	154621	4708	1586	449	841	7007
1351b-61-1-24-27	1093	8658	12782	181562	5201	2022	460	811	7459
1351b-77x-1-33-35	925	14986	12558	138891	3720	1539	496	789	5856
1351b-90-2-113-115	1075	18240	12822	148067	4194	1516	459	906	6090
1351b-97-3-38-40	1072	32413	13360	129551	3968	1735	862	927	4276
1351b-100x-2-39-41	1061	20100	14636	133652	4693	1673	346	1071	5205
1351b-104x-2-13-16	1067	24570	13062	133738	4615	1320	478	1036	4853
1351b-109x-3-6-8	1110	29932	13353	114388	3283	1088	846	1010	5006
1351b-113x-2-100-102	1168	41023	12810	92719	2822	1287	1327	1024	3356
1352b-2h-3-23-25	1050	9067	13266	160278	4924	2137	445	894	6404
1352b-7h-1-73-75	1024	9798	19276	176880	3863	1984	415	633	5296
1352b-12h-1-77-79	958	10390	12500	172590	6139	1821	299	777	6060
1352b-17h-1-44-46	1070	15645	12182	168081	4348	1740	321	750	5897
1352b-23h-5-6-8	948	10061	11934	198608	5437	2264	310	800	6529
1352b-28h-4-49-51	1127	14219	11259	169605	5226	1693	344	884	6179
1352b-37x-2-76-78	1048	32075	13410	144000	4081	1565	1934	947	4650
1352b-42x-4-141-143	1061	19316	13441	140944	4055	1554	475	989	4780
1352b-53x-5-125-127	1135	31114	11873	157655	5728	1920	550	1154	5303
1352b-58x-3-134-136	1192	13060	11997	156429	6089	2012	304	969	6036

Table A.1 Continued

Sample ID	Al	Ca	Cl	Fe	K	Mn	S	Si	Ti
1352b-63x-2-130-132	997	9756	11679	165643	5476	1681	467	1043	6189
1352b-75x-7-10-12	1067	18969	13539	168508	4978	1847	302	863	5471
1352b-81x-2-60-62	1104	88188	11550	72693	2057	862	6561	848	2539
1352c-6r-cc-3-5	1127	23609	11664	183817	6031	1876	370	860	6492
1352c-12r-1-126-128	1001	129418	14658	65933	2047	1012	469	719	2214
1352c-16r-1-12-14	1026	118601	15522	70566	1796	965	537	737	1959
1352c-20r-1-27-29	1184	120822	15554	64968	1599	1125	524	692	2300
1352c-25r-1-128-130	1121	91058	17111	94056	1956	1155	636	776	2847
1352c-30r-2-57-59	1038	10126	26022	26470	67	605	618	673	544
1352c-36r-3-7-9	986	87603	14293	93885	2041	1131	405	675	3073
1352c-41r-3-13-15	963	52599	13435	135244	4570	1195	647	859	4826
1352c-46r-1-34-36	1084	89140	13644	66505	906	1187	502	699	2800
1352c-51r-4-50-52	1106	153067	13593	51398	1255	708	716	748	2233
1352c-57r-1-110-112	1086	120765	15562	76008	2292	831	521	854	2727
1352c-62r-4-9-11	1078	63821	12297	110214	4133	1379	417	1173	4001
1352c-70r-2-5-7	1017	117457	14072	74082	2192	672	545	803	2717
1352c-76r-1-7-9	1050	39683	16417	113677	2103	778	664	774	3829
1352c-85r-1-74-76	1027	95709	14106	73810	1633	773	615	1018	2770
1352c-90r-2-4-6	1133	115271	14259	64794	1645	857	567	925	2194
1352c-95r-4-132-135	1043	57969	23357	63980	1005	798	475	589	2660
1352c-103r-5-132-134	1160	103313	14334	91281	2710	1192	576	834	2969
1352c-107r-3-78-80	1130	90447	17328	79376	1547	948	459	709	2639
1352c-112r-3-31-33	1019	101785	14422	87012	1929	867	575	802	2780
1352c-117r-6-3-5	1005	194354	12131	48583	1183	625	653	876	1938
1352c-124r-4-31-33	966	219952	13170	34250	869	549	882	770	1578
1352c-129r-2-98-100	1122	192357	17764	17502	70	325	680	654	485
1352c-134r-3-116-118	967	256230	11458	15493	284	310	643	547	499
1352c-139r-1-8-10	1092	283398	10799	8210	167	531	719	639	516
1352c-145r-3-1-4	1000	293062	12784	2893	1	271	799	554	439
1352c-148r-1-77-79	1022	259203	13681	8962	372	126	602	703	640

Table A.1 continued

Sample ID	Al	Ca	Cl	Fe	K	Mn	S	Si	Ti
1353b-1h-6-26-28	1041	21266	12811	137719	3364	1598	457	759	5041
1353b-8h-2-91-93	975	13455	12779	190622	5207	2246	393	813	6811
1353b-18x-1-78-80	1034	17756	12460	158226	4760	1794	397	706	5874
1353b-28h-3-6-8	1072	7432	12303	126748	4530	1286	268	982	4904
1353b-40h-2-56-58	958	6186	12822	178146	5565	1685	296	711	6161
1353b-66x-1-90-92	1019	6769	17482	155153	3282	1753	335	773	4777
1353b-71x-1-48-50	1060	10524	12794	143183	4467	1781	720	1011	5070
1353b-75x-1-46-48	1017	6949	12798	138283	4110	1610	446	757	4962
1353b-79x-25-27	1015	8421	17773	133803	3535	1172	376	875	4738
1353b-86x-24-26	1083	6499	12555	123523	4024	1419	418	1026	5179
1353b-90x-25-27	986	6019	17361	124050	2664	1483	404	661	3600
1353b-95x-1-59-61	1054	6895	13082	132251	3943	1322	514	940	4475
1354b-2h-3-49-51	1064	37080	11650	141883	4290	1397	468	1176	5476
1354b-11h-2-8-10	958	9885	11961	191575	5865	2236	343	831	6619
1354b-15h-2-68-70	967	87632	12966	89330	1544	681	526	700	2790
1354c-6x-3-84-86	1070	16727	11936	165135	4566	1655	482	800	5024
1354c-12x-2-53-55	1053	8872	12030	200798	6674	2287	279	869	6881
1354c-18x-3-134	988	7860	11405	194666	6417	1918	442	800	7206
1354c-27x-2-11-13	1074	6067	17933	140489	2199	1367	339	642	3349
1354c-28x-1-84-86	1054	12008	13127	115688	3149	1238	322	918	4125
1354c-36x-1-52-54	1158	16463	13585	133881	2902	1585	335	785	4613
1353b-1h-6-26-28	1041	21266	12811	137719	3364	1598	457	759	5041
1353b-8h-2-91-93	975	13455	12779	190622	5207	2246	393	813	6811
1353b-18x-1-78-80	1034	17756	12460	158226	4760	1794	397	706	5874
1353b-28h-3-6-8	1072	7432	12303	126748	4530	1286	268	982	4904
1353b-40h-2-56-58	958	6186	12822	178146	5565	1685	296	711	6161
1353b-66x-1-90-92	1019	6769	17482	155153	3282	1753	335	773	4777
1353b-71x-1-48-50	1060	10524	12794	143183	4467	1781	720	1011	5070
1353b-75x-1-46-48	1017	6949	12798	138283	4110	1610	446	757	4962
1353b-79x-25-27	1015	8421	17773	133803	3535	1172	376	875	4738

Table A.2

Canterbury Basin Velocimeter Data

Sample ID	Depth (m)	Vel. (m/s)	[a]Vel. Res. (m/s)
1351b-8h-1-117-119	48.87	1812.2	136.3
1351b-16x-2-55-57	114.95	1631.7	-28.1
1351b-21x-1-117-119	161.97	1616.2	-36.4
1351b-27x-2-102-105	220.92	1598	-50.9
1351b-31x-4-24-26	261.44	1620.2	-29.7
1351b-37x-2-51-53	315.91	1622.9	-32.9
1351b-41-1-70-73	353	1706.4	43.5
1351b-47-1-25-28	410.05	1699.8	20.9
1351b-61-1-24-27	524.74	1676.7	-53.6
1351b-77x-1-33-35	668.93	1754.7	-78.6
1351b-90-2-113-115	776.73	1894.2	-45.7
1351b-97-3-38-40	844.78	1811.1	-209.7
1351b-100x-2-39-41	872.19	1903.7	-152.8
1351b-104x-2-13-16	910.43	1866.1	-243.2
1351b-109x-3-6-8	959.86	1932.6	-250.2
1351b-113x-2-100-102	997.6	1904.7	-338.4
1352b-2h-3-23-25	11.43	1671.4	-16.7
1352b-7h-1-73-75	56.43	1598.2	-75.5
1352b-12h-1-77-79	103.97	1594.4	-67.6
1352b-17h-1-44-46	151.14	2837.8	1183.8
1352b-23h-5-6-8	204.76	3629	1979.6
1352b-28h-4-49-51	250.62	1668.3	18.9
1352b-37x-2-76-78	299.26	1595.9	-57.5
1352b-42x-4-141-143	347.01	1640.4	-21.2
1351b-8h-1-117-119	48.87	1812.2	136.3
1351b-16x-2-55-57	114.95	1631.7	-28.1
1351b-21x-1-117-119	161.97	1616.2	-36.4

Table A.2 continued

Sample ID	Depth (m)	Vel. (m/s)	Vel. Res. (m/s)
1352b-58x-3-134-136	497.76	1650.9	-65.0
1352b-63x-2-130-132	545.5	1722	-20.5
1352b-75x-7-10-12	656.9	1761.5	-61.5
1352b-81x-2-60-62	708.2	1770.5	-98.6
1352c-6r-cc-3-5	661.03	1779.1	-47.4
1352c-12r-1-126-128	719.36	1774.8	-105.1
1352c-16r-1-12-14	757.02	3346.5	1428.0
1352c-20r-1-27-29	795.97	3651.65	1690.0
1352c-25r-1-128-130	845.08	3014.9	993.7
1352c-30r-2-57-59	893.87	3159.5	1073.5
1352c-36r-3-7-9	952.47	2776.367	604.9
1352c-41r-3-13-15	1000.43	2219.1	-28.6
1352c-46r-1-34-36	1045.64	3675.2	1350.3
1352c-51r-4-50-52	1097.87	3357.367	936.8
1352c-57r-1-110-112	1151.6	3080.8	554.3
1352c-62r-4-9-11	1203.19	2450.1	-185.4
1352c-70r-2-5-7	1248.25	3099.3	362.7
1352c-76r-1-7-9	1303.97	2612.8	-256.6
1352c-85r-1-74-76	1347.44	3436.8	457.8
1352c-90r-2-4-6	1391.74	3328.8	232.4
1352c-95r-4-132-135	1444.12	2854	-388.6
1352c-103r-5-132-134	1513.42	3344.4	-104.1
1352c-107r-3-78-80	1548.68	3505	-53.8
1352c-112r-3-31-33	1596.73	3135.6	-579.7
1352c-117r-6-3-5	114.95	1631.7	-28.1
1352c-124r-4-31-33	161.97	1616.2	-36.4

Table A.2 continued

Sample ID	Depth (m)	Vel. (m/s)	Vel. Res. (m/s)
1352c-148r-1-77-79	1918.67	4515.9	-439.4
1353b-1h-6-26-28	7.26	1637.5	-52.1
1353b-8h-2-91-93	51.31	1682.4	7.2
1353b-18x-1-78-80	107.38	1711.8	50.5
1353b-28h-3-6-8	152.26	1715.7	61.9
1353b-40h-2-56-58	198.49	1681	31.3
1353b-66x-1-90-92	299.3	1775.4	122.0
1353b-71x-1-48-50	346.48	1799.8	138.3
1353b-75x-1-46-48	384.86	1860.4	189.3
1353b-79x-cc-25-27	423.05	1863.4	179.9
1353b-86x-cc-24-26	490.14	1837.8	125.7
1354b-2h-3-49-51	7.6	1600.6	-88.9
1354b-11h-2-8-10	52.08	1654	-21.0
1354c-6x-3-84-86	95.74	1575.5	-88.3
1354c-12x-2-53-55	146.73	1614.6	-40.0
1354c-18x-3-134-136	206.6	1676.5	27.2
1354c-28x-1-84-86	298.94	1716.9	63.5
1354c-36x-1-52-54	375.12	1796.1	127.7
1352c-148r-1-77-79	1918.67	4515.9	-439.4
1353b-1h-6-26-28	7.26	1637.5	-52.1
1353b-8h-2-91-93	51.31	1682.4	7.2
1353b-18x-1-78-80	107.38	1711.8	50.5
1353b-28h-3-6-8	152.26	1715.7	61.9
1353b-40h-2-56-58	198.49	1681	31.3
1353b-66x-1-90-92	299.3	1775.4	122.0
1353b-71x-1-48-50	346.48	1799.8	138.3

[a]Velocity residuals as measured by Brusova (2010).

REFERENCES

Ackerman, S. A., and Cox, S. K., 1982. The Saudi Arabian heat low: aerosol distribution and thermodynamic structure. *J. Geophys. Res.*, 87: 8991-9002.

Adams, C. J. D., 1979. Age and origin of the Southern Alps. *In* Walcott, R. I., and Cresswell, M. M. (Eds.), *The Origin of the Southern Alps*: Bull.-Roy. Soc. N. Z., 18: 73-78.

Alvarez, L. W., Alvarez, W., Asara, F., and Michel, H. V., 1980. Extraterrestrial cause for the Cretaceous-Tertiary extinction. *Science*, 208, 4448: 1095-1108.

Anderson, D. M., and Prell, W. L., 1991. Coastal upwelling gradient during the late Pleistocene. *In* Stewart, N. J. (Ed.), *Proc. Ocean Drill. Prog.*, 117: College Station, TX (Ocean Drilling Program), 265-276.

Andrews, J. T., Kriby, M. E., Aksu, A., Barber, D., and Meese, D., 1998. Late Quaternary detrital carbonate (DC) layers in Baffin Bay marine sediments (67°-74°): correlation with Heinrich events in the North Atlantic? *Quat. Sci. Rev.*, 17: 1125-1137.

Arimoto, R., 2001. Eolian dust and climate: relationships to sources, tropospheric chemistry, transport and deposition. *Earth Sci. Rev.*, 54: 29-42.

Ayling, B., Rose, P., Petty, S., Zemach, E., and Drakos, P., 2012. QEMSCAN® (Quantitative evaluation of minerals by scanning electron microscopy): capability and application to fracture characterization in geothermal systems. *Proc., Thirty-Seventh Workshop on Geotherm. Reserv. Eng. Stanford University*: Stanford, Calif. (Jan. 30-Feb. 1, 2012 SGP-TR-194).

Batt, G. E., Braun, J., Kohn, B., and McDougall, I., 2000. Thermochronological analysis of the dynamics of the Southern Alps, New Zealand. *Geol. Soc. Am. Bull.*, 112, 2: 250-266.

Blatt, H., Middleton, G. V., and Murray, R., 1980. *Origin of Sedimentary Rocks* (2nd ed.): New Jersey (Prentice Hall).

Bond, G., Heinrich, H., Broecker, W., Labeyrie, L., McManus, J. Andrews, J. Huon, S., Jantschik, R., Clasen, S., Simet, C., Tedesco, K., Klas, M., Bonani, G., and Ivy, S., 1992. Evidence for massive discharges of icebergs into the North Atlantic Ocean during the last glacial period. *Nature*, 360: 245-249.

Broecker, W. S., 1994. Massive iceberg discharge triggers for global climate change. *Nature*, 372: 421-424.

Broecker, W. S., 2003. Does the trigger for abrupt climate change reside in the ocean or in the atmosphere? *Science*, 300: 1519-1522.

Brusova, O., 2010. Compaction of deep sea siliciclastic sediments based on log data [Master Thesis]. Univ. of Utah, Salt Lake City.

Brust, J., and Waniek, J. J., 2010. Atmospheric dust contribution to deep-sea particle fluxes in the subtropical northeast Atlantic. *Deep Sea Res. I*, 57: 988-998.

Burns, S. J., Fleitmann, D., Matter, A., Kramers, J., and Al-Subbary, A. A., 2003. Indian Ocean climate and an absolute chronology over Dansgaard/Oeschger events 9-13. *Science*, 301: 1365-1367.

Cape Roberts Science Team (CRST), 1999. Studies from the Cape Roberts Project, Ross Sea, Antarctica, initial report on CRP-2/2A. *Terra Antarctica*, 6, 1-2: 173.

Carroll, D., 1958. Role of clay minerals in the transportation of iron. *Geochim. Cosmochin. Acta*, 14, 1-2: 1-16.

Carter, L., Carter, R. M., McCave, I. N., and Gambie, J., 1996. Regional sediment recycling in the abyssal southwest Pacific Ocean. *Geology*, 24, 8: 735-738.

Carter, R. M., 2007. The role of intermediate-depth currents in continental shelf-slope accretion: Canterbury Drifts, SW Pacific Ocean. *In* Viana, A. R., and Rebesco, M. (Eds.), *Economic and Paleoceanographic Significance of Contourite Deposits*: Geol. Soc. Spec. Publ., 276, 1: 129-154.

Carter, R. M., and Norris, R. J., 1976. Cenozoic history of southern New Zealand: an accord between geological observations and plate-tectonic predictions. *Earth Planet. Sci. Lett.*, 31, 1: 85-94.

Cesareo, R., 1997. A portable instrument for energy-dispersive X-ray fluorescence analysis of sulfur. *Nucl. Instrum. Meth. Phys. Res.*, Sect. B, 129: 281-283.

Cesareo, R., Gigante, G. E., Castellano, A., and Ridolfi, S., 2009. Portable and handheld systems for energy dispersive X-ray fluorescence analysis. *In* Meyers, R. A. (Ed.), *Encyclopedia of Analytical Chemistry*: New York (John Wiley and Sons, Ltd.).

Cesareo, R., Gigante, G. E., and Ridolfi, S., 2007. Analysis of paintings and alloys with portable EDXRF-equipments. *XRF Newslett.*, Aug. 10-11.

Chao, E. C. T., Shoemaker, E. M., and Madsen, B. M., 1960. First natural occurrence of coesite. *Science*, 132, 3421: 220-222.

Chester, R. 1965. Elemental geochemistry of marine sediments. *In* Riley, J. P., and Skirrow, G. (Eds.), *Treatise on Chemical Oceanography*: New York (Academic Press), 2: 23-80.

Chester, R., and Hughes, M. J., 1966. The distribution of manganese, iron and nickel in a North Pacific deep-sea clay core. *Deep Sea Res.*, 13: 627-634.

Chuhan, F. A., Kjeldstad, A., Bjorlykke, K., and Hoeg, K., 2002. Porosity loss in sand by grain crushing; experimental evidence and relvance to reservoir quality. *Marine and Pet. Geol.*, 19, 1: 39-53.

Chyba, C. F., Thomas, P. J., and Zahnle, K. J., 1993. The 1908 Tunguska explosion: atmospheric disruption of a stony asteroid. *Nature*, 361: 40-44.

Clemens, S.C., and Prell, W. L., 1990. Late Pleistocene variability of Arabian Sea summer monsoon winds and dust source-area aridity: eolian records from the lithogenic component of deep-sea sediments. *Paleoceanography*, 5: 109-145.

Clemens, S. C., and Prell, W. L., 1991. One million year record of summer monsoon winds and continental aridity from the Owen Ridge (Site 722), northwest Arabian Sea. *In* Stewart, N. J. (Ed.), *Proc. Ocean Drill. Prog. Sci. Results*, 117: College Station, TX (Ocean Drilling Program), 365-388.

Clemens, S. C., Prell, W. L., Murray, D., Shimmield, G., and Weedon, G., 1991. Forcing mechanisms of the Indian Ocean monsoon. *Nature*, 353: 720-725.

Clymer, A. K., Bice, D. M., and Montanari, A., 1996. Shocked quartz from the late Eocene: impact evidence from Massignano, Italy. *Geology*, 24: 483-486.

COHMAP Members, 1988. Climatic changes of the last 18,000 years: observations and model simulations. *Science*, 241: 1043-1052.

Corliss, B. H., and Hollister, C. D., 1979. Cenozoic sedimentation in the central North Pacific. *Nature*, 282: 707-709.

Cronin, T. M., 2010. *Paleoclimatology*: New York (Columbia Univ. Press).

Dansgaard, W., Johnsen, S. J., Clausen, H. B., Dahl-Jensen, D., Gundestrup, N., and Hammer, C. U., 1984. North Atlantic climatic oscillations revealed by deep Greenland ice cores. *In* Hansen, J. E., and Takahashi, T. (Eds.), *Climate Processes and Climate Sensitivity*: Washington, D.C. (AGU), 288-298.

Dansgaard, W., Johnsen, S. J., Clausen, H. B., Dahl-Jensen, D., Gundestrup, N., Hammer, C. U., Hridberg, C. S., Steffensen, J. P., Sveinbjörnsdottir, A. E., Jouzel, J., and Bond, G., 1993. Evidence for general instability of past climate from a 250-kry ice-core record. *Nature*, 364: 218-220.

Darwin, C., 1846. An account of the fine dust which often falls on vessels in the Atlantic Ocean. *Q. J. Geol. Soc. London*, 2: 26-30.

Debrabant, P., Krissek, L. A., Bouquillon, A., and Chamley, H., 1991. Clay mineralogy of Neogene sediments of the western Arabian Sea: mineral abundances and paleoenvironmental implications. *In* Stewart, N. J. (Ed.), *Proc. Ocean Drill. Prog. Sci. Results*, 117: College Station, TX (Ocean Drilling Program), 183-196.

Dixon, J. B., and Weed, S. B., 1977. *Minerals in Soil Environments*: Madison, WI (Soil Sci. Soc. of Am.).

Doyle, P., 1980. Seabed disposal program: improvement of ichthyolith stratigraphy for Giant Piston Core 3. *Progress Report, Sandia Laboratories*.

Doyle, P. S., and Riedel, P. S., 1979. Cretaceous to Neogene ichthyoliths in a giant piston core from the Central North Pacific. *Micropaleontology*, 25, 4: 337-364.

Dymond, J., Corliss, J. B., Heath, G. R., Field, C. W., Dasch, E. J., and Veeh, H. H., 1973. Origin of metalliferous sediments from the Pacific Ocean. *Geol. Soc Am. Bull.*, 84: 3355-3372.

Economou, T., Turkevich, A., Rieder, R., and Wanke, H., 1996. Chemical composition of Martian surface and rocks on Pathfinder Mission. *Lunar Planet. Sci. Conf.*, 27: 1111-1112.

Erickson, S. N., and Jarrard, R. D., 1998. Velocity-porosity relationships for water-saturated siliciclastic sediments. *J. Geophys. Res.*, 103: 30385-30406.

Expedition 317 Scientists, 2011. Expedition 317 Summary. *In* Fulthorpe, C. S., Hoyanagi, K., Blum, P., and the Expedition 317 Scientists, *Proc. IODP*, 317: Tokyo (Integrated Ocean Drilling Program Management International, Inc.).

Farley, K. A., Montanari, A., Shoemaker, E. M., and Shoemaker, C. S., 1998. Geochemical evidence for acomet shower in the late Eocene. *Science*, 280, 5367: 1250-1253.

Field, B. D., and Browne, G. H., 1989. *Cretaceous and Cenozoic Sedimentary Basins and Geological Evolution of Canterbury Region, South Island, New Zealand* (No. 2): Geol. Surv., Basin Stud., 2.

Fisher, R. A., and Yates, F., 1948. *Statistical Tables for Biological, Agricultural and Medical Research* (3rd ed.): Edinburgh (Oliver and Boyd).

Fleming, C. A., 1962. New Zealand biogeography: a paleontologist's approach. *Tuatara*, 10: 53-108.

Foscolos, A. E., 1990. Catagenesis of argillaceous sedimentary rocks. *In* McIlreath, I. A., and Morrow, D. W (Eds.), *Diagenesis*: Ottawa, Ont. (Runge Press), 177-187.

Friedman, G. M., and Sanders, J. E., 1978. *Principles of Sedimentology*: New York (John Wiley and Sons).

Fulthorpe, C. S., and Carter, R. M., 1989. Test of seismic sequence methodology on a Southern Hemisphere passive margin: the Canterbury Basin, New Zealand. *Mar. Pet. Geol.*, 6, 4: 348-359.

Gayraud, J., Robin, E., Rocchia, R., and Froget, L., 1996. Formation conditions of oxidized ni-rich spinel and their relevance to the K/T boundary event. *Geolog. Soc. Am. Spec. Papers*, 307: 425-443.

Gibbs, R. J., 1967. Quantitative X-ray diffraction analysis using clay mineral standards extracted from the samples to be analyzed. *Clay Min.*, 7: 79-90.

Gillete, D. A., Blifford, I. H., Jr., and Fryrear, D. W., 1974. The influence of wind velocity on the size distribution of aerosols generated by the wind erosion of soils. *J. Geophys. Res.*, 79: 4068-4075.

Glass, B. P., and Koeberl, C., 1999. ODP Hole 689B spherules and upper Eocene microtektite and clinopyroxene-bearing spherule strewn fields. *Meteorit. Planet. Sci.*, 34: 247-258.

Glass, B. P., and Zwart, M. J., 1977. North American microtektites radiolarian extinctions and the age of the Eocene-Oligocene boundary. *In* Swain, F. M. (Ed.), *Stratigraphic Micropaleontology of the Atlantic Basin and Borderlands*. Amsterdam (Elsevier), 553-568.

Glass, B. P., Burns, C. A., Crosbie, J. R., and Dubois, D. L., 1985. Late Eocene North American microtektites and clinopyroxene-bearing spherules. *Proc. Lunar Planet. Sci. Conf.*, 16: D175-D196.

Goldberg, E. D., 1954. Marine geochemistry I. chemical scavengers of the sea. *J. Geol.*, 62: 249-265.

Goldberg, E. D., and Griffin, J. J., 1970. The sediments of the northern Indian Ocean. *Deep Sea Res.*, 17: 513-537.

Goldstein, J., Newbury, D., Joy, D., Lyman, C., Echlin, P., Litshin, E., Sawyer, L., and Michael, J., 2002. *Scanning Electron Microscopy and X-ray Microanalysis* (2rd ed.): New York (Kluwer Academic/Plenum Publishers).

Gottlieb, P., Wilkie, G., Sutherland, D., Ho-Tun, E., Suthers, S., Perera, K., Jenkins, B., Spencer, S., Butcher, A., and Rayner, J., 2000. Using quantitative electron microscopy for process mineralogy applications. *J. Minerals, Metals, and Materials Soc.*, 52, 4: 24-25.

Goudie, A. S., 1983. Dust storms in space and time. *Prog. Phys. Geogr.*, 7: 502-530.

Haberlah, D., Williams, M. A. J., Halverson, G., Hrstka, T., Butcher, A. R., McTainsh, G. H., Hill, S. M., and Glasby, P., 2010. Loess and floods: high-resolution multi-proxy data of Last Glacial Maximum (LGM) slackwater deposition in the Flinders Ranges, semi-arid South Australia. *Quat. Sci. Rev.*, 29, 19-20: 2673-2693.

Hastenrath, S., and Lamb, P. J., 1979. *Climatic Atlas of the Indian Ocean*: Madison, WI (Univ. of Wisconsin Press).

Hayes, J. B., 1979. Sandstone diagenesis – the hole truth. *In* Scholle, P. A., and Schluger, P. R. (Eds.), *Aspects of Diagenesis*. Spec. Publ. Soc. Econ. Paleontol. Mineral., 26: 127-139.

Heath, G. R., 1969. Mineralogy of Cenozoic deep-sea sediments from the equatorial Pacific Ocean. *Geol. Soc. Am. Bull.*, 80: 1997-2018.

Heinrich, H., 1988. Origin and consequence of cyclic ice rafting in the northeast Atlantic Ocean during the past 130,000 years. *Quat. Res.*, 29: 142-152.

Hemming, S. R., 2004. Heinrich events: massive late Pleistocene detritus layers of the North Atlantic and their global climate imprint. *Rev. Geophys.*, 42: 1-43.

Hughen, K. A., Southon, J. R., Lehman, S. J., and Overpeck, J. T., 2000. Synchronous radiocarbon and climate shifts during the last deglaciation. *Science*, 290: 1951-1954.

Hutcheon, I., 1990. Aspects of the diagenesis of coarse-grained siliciclastic rocks. *In* McIlreath, I. A., and Morrow, D. W. (Eds.), *Diagenesis*: Ottawa, Ont. (Runge Press), 165-176.

Janacek, T. R., and Rea, D. K., 1983. Eolian deposition in the northeast Pacific Ocean: Cenozoic history of atmospheric circulation. *Geol. Soc. Am. Bull.*, 94: 730-738.

Jarrard, R. D., Niessen, F., Brink, J. D., and Bücker, C., 2000. Effects of cementation on velocities of siliciclastic sediments. *Geophys. Res. Lett.*, 27, 5: 593-596.

Jenkins, B. M., Zhu, R., and Esterle, J., 1995. Ergodicity: the challenge of sampling for automated microscopy in the minerals industry. *Proc. Digital Image Computin: Techniques and Applications*: Brisbane, Australia (APRS), 401-407.

Johnson, L. R., 1979. Mineralogical dispersal patterns of North Atlantic deep-sea sediments with particular reference to eolian dusts. *Marine Geology*, 29: 334-345.

Kassler, P., 1973. The structural and geomorphic evolution of the Persian Gulf. *In* Purser, B. H. (Ed.), *The Persian Gulf*: New York (Springer-Verlag), 11-32.

Kienast, M., Steinke, S., Stattegger, K., and Calvert, S. E., 2001. Synchronous tropical South China Sea SST change and Greenland warming during deglaciation. *Science*, 291: 2132-2134.

King, P. R., 2000. Tectonic reconstructions of New Zealand: 40 Ma to the present. *N. Z. J. Geol. Geophys.*, 43: 611-638.

King, R. P., and Schneider, C. L., 1998. Stereological correction of linear grade distributions for mineral liberation. *Powder Technology*, 98, 1: 21-37.

Kohfeld, K. E., and Harrison, S. P., 2001. DIRTMAP: the geological record of dust. *Earth Sci. Rev.*, 54: 81-114.

Kolla, V., Henderson, L., and Biscaye, P. E., 1976. Clay mineralogy and sedimentation int eh western Indian Ocean. *Deep Sea Res. Oceanogr. Abstr.*, 23: 949-961.

Kolla, V., Kostecki, J. A., Robinson, F., Biscaye, P. E., and Ray, P. K., 1981. Distribution and origins of clay minerals and quartz in surface sediments of the Arabian Sea. *J. Sediment. Petrol.*, 55: 37-41.

Krissek, L. A., 1982. Sources, dispersal, and contributions of fine-grained terrigenous sediments on the Oregon and Washington continental slope [Ph.D. dissert.] Oregon State Univ., Corvallis.

Krissek, L. A., and Clemens, S. C., 1991. Mineralogic variations in a Pleistocene high-resolution eolian record from the Owen Ridge, western Arabian Sea (Site 722): implications for sediment source conditions and monsoon history. *In* Stewart, N. J. (Ed.), *Proc. Ocean Drill. Prog. Sci. Results*, 117: College Station, TX (Ocean Drilling Program), 197-211.

Kuenen, P., 1958. No geology without marine geology. *Geol. Rundschau*, 47: 1-10.

Kukla, G. Heller, F., Ming, L. X., Chan, X. T., Sheng, L. T., and Sheng, A. Z., 1988. Pleistocene climates in China dated by magnetic susceptibility. *Geology*, 16: 811-814.

Kutzbach, J. E., 1981. Monsoon climate of the early Holocene: climate experiment with the Earth's orbital parameters for 9000 years ago. *Science*, 214: 59-61.

Kutzbach, J. E., and Guetter, P. J., 1986. The influence of changing orbital parameters and surface boundary conditions on climate simulations for the past 18,000 years. *J. Atmos. Sci.*, 43, 16: 1726-1759.

Kutzbach, J. E., and Otto-Bliesner, B. L., 1982. The sensitivity of the African-Asian monsoonal climate to orbital parameter changes for 9000 years B.P. in a low-resolution General Circulation Model. *J. Atmos. Sci.*, 39: 1177-1188.

Laevastu, T., and Mellis, O., 1955. Extraterrestrial material in deep-sea deposits. *Trans. Am. Geophys. Un.*, 36: 385-389.

Landergren, S., 1964. On the geochemistry of deep-sea sediments. *Rep. Swed. Deep Sea Exped.*, 10, 5: 57-154.

Leinen, M., and Heath, G. R., 1981. Sedimentary indicators of atmospheric activity in the northern hemisphere during the Cenozoic. *Paleogeogr. Palaeoclimatol. Palaeoecol.*, 36: 1-21.

Li, C., and Yanai, M., 1996. The onset and Interannual variability of the Asian summer monsson in relation to land-sea thermal contrast. *J. Clim.*, 9: 358-375.

Lisitzen, A. P., 1972. Sedimentation in the world ocean with emphasis on the nature, distribution, and behavior of marine suspensions. *Spec. Publ. Soc. Econ. Paleontol. Mineral.*, 17: 218 pp.

Lu, H., Fulthorpe, C.S., Mann, P., and Kominz, M., 2005. Miocen-recent tectonic and climate controls on sediment supply and sequence stratigraphy: Canterbury Basin, New Zealand. *Basin Res.*, 17, 2: 311-328.

Magara, K., 1980. Comparison of porosity-depth relationships of shale and sandstone. *J. Pet. Geol.*, 3: 175-185.

Maher, B. A., Prospero, J. M., Mackie, D., Gaiero, D., Hesse, P. P., and Balkanski, Y., 2010. Global connections between Aeolian dust, climate and ocean biogeochemistry at the present day and at the last glacial maximum. *Earth Sci. Rev.*, 99: 61-97.

Mahowald, N., Kohfeld, K., Hansson, M., Balkanski, Y., Harrison, S. P., Colin Prentice, I., Schulz, M., and Rodhe, H., 1999. Dust sources and deposition during the last glacial maximum and current climate: a comparison of model results with paleodata from ice cores and marine sediments. *J. Geophys. Res.*, 104, D13: 15895-15916.

Marabelli, M., Santpadre, P., Ioele, M., Bianchetti, P. L., Castellano, A., and Cesareo, R., 2005. Giotto's painting techniques in the Scrovegni Chapel: a study of the materials. *Bollettino d'arte, volume special: Giootto in the Scrovegni Chapel*, *Istituto poligrafico dello Stato*, 17-47.

Martin, W., Baross, J., Kelley, D., and Russell, M. J., 2008. Hydrothermal vents and the origin of life. *Nature Rev. Microbiology*, 6: 805-814.

Maury, M. F., 1855. *The Physical Geography of the Sea* (3rd ed.): New York (Harper and Brothers Publishers).

McDonald, W. F., 1938. *Atlas of Climatic Charts of the Oceans*: Washington, D.C. (U.S.D.A., Weather Bur.), charts 59-62.

Mermut, A. R., and Cano, A. F., 2001. Baseline studies of the clay minerals society source clays: chemical analyses of major elements. *Clays and Clay Minerals*, 49, 5: 381-386.

Middleton, N. J., 1985. Effect of drought on dust production in the Sahel. *Nature*, 316: 431-434.

Molnar, P., Atwater, T., Mammerickx, J., and Smith, S., 1975. Magnetic anomalies, bathymetry and the tectonic evolution of the South Pacific since the late Cretaceous. *Geophys. J. R. Astron. Soc.*, 40: 383-420.

Montanari, A., Asaro, F., Michel, V. H., and Kennett, J. P., 1993. Iridium anomalies of late Eocene age at Massignano (Italy), and ODP Site 689B (Maud Rise, Antarctic). *Palaios*, 8: 420-437.

Morris, M., Stanton, B., and Neil, H., 2001. Subantarctic oceanography around New Zealand: preliminary results from an ongoing survey. *N. Z. J. Mar. Feshwater Res.*, 35: 499-519.

Mountain, G. S., and Prell, W. L., 1989. Geophysical reconnaissance for ODP leg 117 in the northwest Indian Ocean. *In* Prell, W. L., Niitsuma, N., et al., *Proc. ODP Init. Repts.*, 117: College Station, TX (Ocean Drilling Program), 51-64.

Nair, K. R., 1940. Table of confidence interval for the median in samples from any continuous population. *Proc. Indian Statis. Conf.*, 4, 4: 551-558.

Nair, R. R., Ittekkot, V., Manganini, S. J., Ramaswamy, V., Haake, B., Degens, E. T., Desui, B. N., and Honjo, S., 1989. Increased particle flux to the deep ocean related monsoons. *Nature*, 338: 749-751.

Nazaroff, A. J., Prufer, K. M., and Drake, B. L., 2010. Assessing the applicability of portable X-ray fluorescence spectrometry for obsidian provenance research in the May lowlands. *J. Archaeo. Sci.*, 37, 4: 885-895.

Nicholson, S. E., 1985. Sub-Saharan rainfall 1981-1984. *J. Clim. Appl. Meteorol.*, 24: 1388-1391.

Niessen, F., Kopsch, C., and Polozek, K., 2000. Velocity and porosity from CRP-2/2A core logs, Victoria Land Basin, Antarctica. *Terra Antarctica*, 7, 3: 241-253.

Norris, R. J., Carter, R. M., and Turnbull, L. M., 1978. Cainozoic sedimentation in basins adjacent to a major continental transform boundary in southern New Zealand. *J. Geol. Soc. (London, U. K.)*, 135, 2: 191-205.

O'Keefe, J. A., 1970. Tektite glass in Apollo 12 sample. *Science*, 168, 3936: 1209-1210.

Oeschger, H., Beer, J., Siegenthaler, U., Stauffer, B., Dansgaard, W., and Langway, C., 1984. Late glacial climate history from ice cores. *In* Hansen, J. E., and Takahashi, T. (Eds.), *Climate Processes and Climate Sensitivity*: Washington, D.C. (AGU), 299-306.

Pettersson, H., 1959. Manganese and nickel on the ocean floor. *Geochim. Cosmochin. Acta*, 17: 209-213.

Pierazzo, E., and Artemieva, N., 2012. Impact!: local and global environmental effects of impacts on Earth. *Elements*, 8, 1: 55-60.

Pierrard, O., Robin, E., Rocchia, R., and Montanari, A., 1998. Extraterrestrail ni-rich spinel in upper Eocene sediments from Massignano, Italy. *Geology*, 26: 307-310.

Pierrard, O., Robin, E., Rocchia, R., Leferre, I., Smit, J., G. E. A. / C. N. R. S., Vonhof, H., 1999. Late Eocene ni-rich spinel from LL44-GPC3 (Central Pacific), ODP site 689B (Maud Rise, Antarctic), DSDP sites 94 (Gulf of Mexico) and 612 (US East Coast). *Lunar and Planet. Sci.*, 30: 1674.

Pope, K. O., Baines, K. H., Ocampo, A. C., and Ivanov, B. A., 1994. Impact winter and the Cretaceous/Tertiary extinctions: results of a Chixulub asteroid impact model. *Earth Planet. Sci. Lett.*, 128, 3-4: 719-725.

Prell, W. L., 1984a. Variation of monsoonal upwelling: a response to changing solar radiation. *In* Hansen, J. E., and Takahashi, T. (Eds.), *Geophys. Mongr. Ser. Climate Processes and Climate Sensitivity*: Washington, D.C. (AGU), 29: 48-57.

Prell, W. L., 1984b. Monsoonal climate of the Arabian Sea during the late Quaternary: a response tochanging solar radiation. *In* Berger, A. L., Imbrie, J., Hays, J., Kukla, G., and Saltzman, B. (Eds.), *Milankovitch and Climate* (Pt. I): Dordrect (D. Reidel), 349-366.

Prell, W. L., and van Campo, E., 1986. Coherent response of Arabian Sea upwelling and pollen transport to late Quaternary monsoonal winds. *Nature*, 323: 526-528.

Prince, R., Heath, G. R., and Kominz, M., 1980. Paleomagnetic studies of central North Pacific sediment cores: stratigraphy, sedimentation rates, and the origin of magnetic instability. *Geolog. Soc. Am. Bull.* (Pt. 2), 91: 1789-1835.

Prodi, F., Santachiara, G., and Oliosi, F., 1983. Characterization of aerosols in marine environments (Mediterranean, Red Sea, and Indian Ocean). *J. Geophys. Res.*, 88: 10957-10968.

Prospero, J. M., 1981. Arid regions as sources of mineral aerosols in the marine atmosphere. *In* Péwé, T. L. (Ed.), *Desert Dust-Origin, Characteristics, and Effects on Man*: Spec. Pap. –Geol. Soc. Am., 186: 71-86.

Prospero, J. M., Uematsu, M., and Savoie, D. L., 1989. Mineral aerosol transport to the Pacific Ocean. *In* Riley, J. P., Chester, R., and Duce, R.A. (Eds.), *Chemical Oceanography*: San Diego, CA (Academic Press), 10: 187-218.

Pye, K., 1987. *Aeolian Dust and Dust Deposits*: New York (Academic Press), 97-98.

Pye, K., 1989. Processes of fine particle formation, dust source regions, and climatic changes. *In* Leinen, M., and Sarnthein, M. (Eds.), *Paleoclimatology and Paleometeorology:Modern and Past Patterns of Global Atmospheric Transport*: Norwell, Mass. (Kluwer Academic), 3-30.

Rea, D. K., 1994. The paleoclimatic record provided by eolian deposition in the deep sea: the geologic history of wind. *Rev. Geophysics*, 32, 2: 159-195.

Rea, D. K., Leinen, M., Janacek, T. R., 1985. Geologic approach to the long-term history of atmospheric circulation. *Science*, 227: 721-725.

Rhodes, J. R., 1971. *Design and application of X-ray emission analyzers using radiosisotop X-ray or gamma ray sources*: American Soc. for Testing and Materials, Special Technical Publication 243, 485.

Robin, E., Bonté, Ph., Froget, L., Jéhanno, C., and Rocchia, R., 1992. Formation of spinels in cosmic objects during atmospheric entry: a clue to the Cretatceous-Tertiary boundary event. *Earth Planet. Sci. Lett.*, 108, 4: 181-190.

Sarnthein, M., Thiede, J., Pflaumann, U., Erlenkeuser, H., Futterer, D., Koopmann, B., Lange, H., and Seibold, E., 1982. Atmospheric and oceanic circulation patterns off northwest Africa during the past 25 million years. *In* von Rad, U. et al. (Eds.), *Geology of the Northwest African Continental Margin*: New York (Springer-Verlag), 545-604.

Savoie, D. L., prospero, J. M., and Nees, R. T., 1987. Nitrate, no-sea-salt sulfate, and mineral aerosol over the northwestern Indian Ocean. *J. Geophys. Res.*, 92: 933-942.

Scheidegger, K. F., and Krissek, L. A., 1982. Dispersal and deposition of eolian and fluvial sediments off Peru and northern Chile. *Geol. Soc. Am. Bull.*, 93: 150-162.

Sendova, M., Kaiser, B., Scalera, M., and Zhelyaskov, V., 2010. Della Robbia blue glaze: micro-Raman temperature study and X-ray fluorescence spectroscopy characterization. *J. Raman Spectrosc.*, 41, 4: 469-472.

Shipboard Scientific Party, 1989. Site 722. *In* Prell, W. L., Niitsuma, N., et al., *Proc. ODP Init. Repts.*, 117: College Station, TX (Ocean Drilling Program), 255-318.

Sirocko, F., and Sarnthein, M., 1989. Wind-borne deposits in the northwest Indian Ocean: record of Holocene sediments versus modern satellite data. *In* Leinen, M., and Sarnthein, M. (Eds.), *Paleoclimatology and Paleometeorology: Modern and Past Patterns of Global Atmospheric Transport*: NATO ASI Ser., 282: 401-433.

Speakman, R. J., Little, N. C., Creel, D., Miller, M. R., and Iñañez, J. G., 2011. Sourcing ceramics with portable XRF spectrometers? A comparison with INAA using Mimbres pottery from the American Southwest. *J. Archaeo.Sci.*, 38, 12: 3483-3496.

Stoll, R. D., 1989. *Sediment Acoustics*: Berlin (Springer-Verlag).

Street, A. F., and Grove, A. T., 1979. Global maps of lake-level fluctuations since 30,000 yr B.P. *Quat. Res.*, 12: 83-118.

Stuut, J. W., Prins, M. A., Schneider, R. R., Weltje, G. J., Fred Jansen, J. H., and Postma, G., 2002. A 300-kyr record of aridity and wind strength in southwestern Africa: inferences from grain-size distributions of sediments on Walvis Ridge, SE Atlantic. *Marine Geology*, 180: 221-233.

Taft, B. A., Ramp, S. R., Dworski, J. G., and Holloway, G., 1981. Measurements of deep currents in the central North Pacific. *J. Geophys. Res.*, 86: 1955-1968.

Taylor, J. M., 1950. Pore space reduction in sandstones. *AAPG Bull.*, 23: 701-717.

Taylor, S. R., 1973. Tektites: a post-Apollo view. *Earth Sci. Rev.*, 9, 2: 101-123.

Till, R., and Spears, D. A., 1969. The determination of quartz in sedimentary rocks using an X-ray diffraction method. *Clays and Clay Mineral.*, 17: 323-327.

Tippett, J. M., and Kamp, P. J. J., 1993a. Fission track analysis of the late Cenozoic vertical kinematics of continental Pacific crust, South Island, New Zealand. *J. Geophys. Res.*, [*Solid Earth Planet*], 98, 9: 16119-16148.

Tippett, J. M., and Kamp, P. J. J., 1993b. The role of faulting in rock uplift in the Southern Alps, New Zealand. *N. Z. J. Geol. Geophys.*, 36, 4: 497-504.

Tsoar, H., and Pye, K., 1987. Dust transport and the question of desert loess formation. *Sedimentology*, 34: 139-153.

van Campo, E., 1986. Monsoon fluctuations in two 20,000-yr B.P. oxygen-isotope/pollen records off southwest India. *Quat. Res.*, 26: 376-388.

van Campo, E., Duplessy, J. C., and Rossignol-Strict, M., 1982. Climatic conditions deduced from a 150-kyr oxygen isope-pollen record from the Arabian Sea. *Nature*, 296: 56-59.

Velde, B., 1985. *Clay Minerals: A Physico-Chemical Explanation of Their Occurrence*: Amsterdam (Elsevier).

Vonhof, H. B., and Smit, J., 1999. Late Eocene microkrystites at Maud Rise (Ocean Drilling Project Hole 689B; Southern Ocean) suggest a global extension of the approximately 35.5 Ma Pacific impact ejecta strewn field. *Meteorit. Planet. Sci.*, 34: 747-755.

Wang, Y. J., Cheng, H., Edwards, R. L., et al., 2001. A high-resolution absolute-dated late Pleistocene monsoon record from Hulu Cave, China. *Science*, 294: 2345-2348.

Weaver, H. A., A'Hearn, M. F., Arpigny, C., Boice, D. C., Feldman, P. D., Larson, S. M., Lamy, P., Levy, D. H., Marsden, B. G., Meech, K. J., and al. et, 1995. The Hubble Space Telescope (HST) observing campaign on comet Shoemaker-Levy 9. *Science*, 267, 5202: 1282-1288.]

Webster, P. J., 1987. The elementary monsoon. *In* Fein, J. S., and Stephens, P. L. (Eds.), *Monsoons*: New York (Wiley), 3-32.

Wellman, H. W., 1971. Age of the Alpine Fault, New Zealand. *Proc. Int. Geol. Congr. 22nd*, 4: 148-162.

Weser, O. E., 1974. Sedimentological aspects of strata encountered in leg 23 in the northern Arabian Sea. *Initial Rep. Deep Sea Drill. Proj.*, 23: 503-519.

Wyllie, M. R. J., Gregory, A. R., and Gardner, L. W., 1956. Elastic wave velocities in heterogenous and porous media. *Geophysics*, 21: 41-70.